



# Turbo-assisted direct solar air heater for medium temperature industrial processes using Linear Fresnel Collectors. Assessment on daily and yearly basis



Antonio Famiglietti <sup>a,\*</sup>, Antonio Lecuona <sup>a</sup>, Mercedes Ibarra <sup>b,c</sup>, Javier Roa <sup>d</sup>

<sup>a</sup> Universidad Carlos III de Madrid, Departamento de Ingeniería Térmica y de Fluidos, Avda. de La Universidad 30, 28911, Leganés, Madrid, Spain

<sup>b</sup> Fraunhofer Chile Research – Center for Solar Energy Technologies, Vicuña Mackenna, 4860, Santiago, Chile

<sup>c</sup> E.T.S. Ingenieros Industriales, Universidad Nacional de Educación a Distancia (UNED), C/Juan Del Rosal 12, Madrid, Spain

<sup>d</sup> Demede Engineering and Research, Laguna de Marquesado 47 Nave K Polígono Villaverde, 28021, Madrid, Spain

## ARTICLE INFO

### Article history:

Received 29 June 2020

Received in revised form

25 January 2021

Accepted 28 January 2021

Available online 3 February 2021

### Keywords:

Solar heat for industrial processes

Linear Fresnel collectors

Direct solar air heating

Solar Brayton cycle

Industrial drying

## ABSTRACT

The study analyzes an innovative concentrating solar thermal system aimed at the direct production of hot air for industrial applications. Air is heated inside linear Fresnel collectors in an open to atmosphere circuit, not requiring the use of a primary heat transfer fluid and a heat exchanger, with their associated cost and maintenance. Matching an automotive turbocharger with the solar field avoids auxiliary energy consumption for pumping the airflow. The detailed quasi-steady numerical model implemented, including commercial collector and turbocharger technical features, allows to scrutinize the daily and yearly operating time profile of a medium scale plant with a 633.6 m<sup>2</sup> solar field. Considering the typical meteorological year of the selected location (Madrid, Spain), the numerical results indicate that hot air is provided at a remarkable quasi-constant temperature between 300 °C and 400 °C despite the solar variations, delivering 330 MW h per year without overheating the receiver evacuated tubes.

© 2021 Elsevier Ltd. All rights reserved.

## 1. Introduction

The industrial sector is responsible for one-third of global energy consumption [1]. Process heat has a substantial share of industrial energy demand, required at different temperature levels. According to Refs. [2,3], heat has the 74% share of industrial world energy demand corresponding to 85 Exajoule, almost totally provided by fossil fuel. The 30% of heat demand is in the low temperature range ( $T < 150$  °C), 22% in the medium temperature range ( $150$  °C  $< T < 400$  °C) and 48% in the high temperature range ( $T > 400$  °C). Sharma et al. [4] reported that conventional heating in industries follows two primary heating practices: combustion-based and electricity-based facilities. In most of applications heat is transferred to the material using a Heat Transfer Fluid (HTF). Common HTFs used in the industry range from thermal oil, saturated steam, superheated steam, pressurized hot water and air.

Industrial processes using hot air as HTF are widespread and operate in several industrial sectors, Table 1 reports some of them.

Drying is one of the high energy-demanding processes, being customary to heat air in order to increase its water removal capacity. Pirasteh et al. [5] provided a detailed review of drying in industrial processes and agriculture. Wu et al. [6] reviewed the drying techniques in the mineral processing industry.

Hot air is provided mostly by consuming fossil fuel or electricity. Electricity has only a partial renewable source share, which is intermittent, it is grid-dependent and frequently produced far away. The global efforts for climate preservation and pollutant emission reduction aim at replacing fossil fuel with clean renewable energy sources. Due to their high efficiency and the ubiquity of the sun, Solar Heat for Industrial Processes (SHIP) offers enormous potential for decarbonization. Sharma et al. [4] and Kumar et al. [7] reviewed the SHIP state of the art. Farjana et al. [8] presented a comprehensive review, analyzing industrial processes that could adopt solar sources. They mainly reported low-temperature processes.

Flat Plate Collectors (FPCs) and Evacuated Tube collectors (ETCs) are suitable solutions for low-temperature applications (below 100 °C). Working with a primary HTF in a closed-loop, they need an HTF/air Heat eXchanger (HX) to heat the process air. However, Solar Air Heating (SAH) is also possible directly inside the solar air

\* Corresponding author.

E-mail address: [antonio\\_famiglietti@live.it](mailto:antonio_famiglietti@live.it) (A. Famiglietti).

**Table 1**  
Thermal processes using air as HTF. \* own research, air temperature.

Sector	Process	Temperature [°C]	Source
Food & Beverage	Drying, dehydration	40–100	[4]
"	Washing, cleaning	40–80	[4]
"	Pasteurization, sterilization	70–100	[13]
"	Concentration	70 - 150*	[13]
Pulp and paper	Drying	90–200	[4]
Chemical and pharmaceutical	Drying	120–170	[4]
Rubber	Drying	50–130	[4]
Glass	Drying	150–175	[4]
Manufacturing	Laminating	100–180	[4]
Casting	Hardening, annealing, tempering, forging, rolling	200–700	[4]
Cement	Lime calcining	600–1200	[4]
Automobile	Paint drying and curing	200–300	[8]
Water treatment	Desalination	200 - 300*	[13]
Blackwater purification	Sludge drying	200 - 300*	Own research

collector (AC) [9], avoiding HTF leakage problems, fire risks, and recycling costs. Although customarily limited to the low-temperature range, several applications use SAHs of the Open to Atmosphere Circuit (OAC) type for industrial drying [8], especially for food drying.

Concentrating collectors allow reaching higher temperatures than ACs, FPCs, or ETCs, up to 500 °C. Low-cost modules for SHIP applications of both Linear Fresnel Collectors (LFCs) and Parabolic Trough Collectors (PTCs) are commercially available. Sharma et al. [4] reported several existing industrial Concentrating Solar Heat (CSH) plants around the world. The SHIP database [10] reported 13 plants using LFCs for SHIP, from 123 m<sup>2</sup> of area up to 2000 m<sup>2</sup>, with a delivery temperature below 225 °C. Several of them use pressurized water as the primary HTF for process heat, or industrial refrigeration when directly coupled with absorption chillers. 58 projects were reported using PTC in this database, with solar field areas from 34 m<sup>2</sup> to 5060 m<sup>2</sup>, except for the large Miraah Oman project for steam generation. Oil, steam, and water are used as HTF, while applications go from process heating and steam generation, cooking, and water desalination. Farjana et al. [8] also reported examples of CSH installation using PTCs for different purposes: water heating (95 °C) preheating processes (95 °C), steam-driven processes (130–243 °C), pasteurization (80–95 °C), drying and cooking (40–95 °C), food processing (150 °C), and space heating. Applications of linear concentrating collectors for direct process air heating are rare, and all the reported ones use a primary liquid HTF. One example, reported by Ref. [10], operates in a car paint shop for coat drying in Germany. An LFC solar field of 132 m<sup>2</sup> reflecting area heats water up to 180 °C producing hot air through a water/air heat exchanger integrated with a natural gas boiler for additional heat supply. The SHIP database [10] reported another example in Portugal, with a field of 105 m<sup>2</sup> of PTCs. Thermal oil is heated up to 160 °C to process finished products using air. Another example was reported by Ref. [11], a 102 kW rated thermal capacity LFC system operates with thermal oil as primary HTF, heating an airflow through an oil/air heat exchanger up to 180 °C. Air is then used in an indirect evaporative cooling unit. Maximum effectiveness of oil/air heat exchanger of 0.8–0.9 was found.

Famiglietti et al. [12] presented an innovative concept for directly heating ambient air up to a medium temperature of 300 °C–400 °C in an Open to Atmosphere Circuit (OAC) using linear concentrating collectors. The concentrating solar air heater proposed avoids the use of a primary HTF and the HTF/air heat exchanger, reducing potential cost and environmental impact. One of the main drawbacks of straight direct air heating is the high pumping power needed to drive air through the solar field, because of high airflow velocities, especially for long collector rows with a

high solar concentration ratio. To overcome this drawback, in that study an original Brayton cycle configuration was proposed, using an automotive turbocharger to reduce the total pressure drops across the solar field, besides extracting the required pumping power from the high enthalpy of the heated and pressurized air, avoiding or minimizing the auxiliary pumping energy demand. The authors analyzed the proposed Solar Air Heater assisted by a Turbocharger (T-SAH) from a theoretical point of view, investigating the effect of basic independent parameters (concentrated irradiance, collector length, compression ratio, mass flow rate, turbine and compressor efficiencies) on the operating conditions of a generic system at arbitrary operating conditions, to ascertain its viability. Moreover, to keep general validity, they didn't restrict their analysis to a specific collector type (PTC or LFC) or solar field size and configuration, or specific turbocharger; only a parametric study was performed.

In the present study, the concept of T-SAH originally proposed in Ref. [12] is applied to a medium-scale solar facility for hot air production in industry using LFCs. The numerical model implemented incorporates the technical features of commercial LFCs and turbochargers, as well as real solar and ambient conditions. This allows the evaluation of its time performances comprehensively under variable solar resources on a daily and yearly basis, thus under off-design conditions, not addressed in previous literature. Pressure ratio and mass flow rate varies along the day according to solar input and ambient temperature. Surprisingly, the outlet air temperature is quite steady, which is highly advantageous and not previously documented.

## 2. Turbo-assisted solar air heater T-SAH

Direct air heating inside linear concentrating collector was parametrically analyzed by Ref. [12]. The authors highlighted that air presents physical properties that difficult the heat evacuation from the solar collector receiver tube. The relatively low thermal conductivity, as well as the high kinematic viscosity at low pressures, turns into a modest internal wall-to-flow heat transfer coefficient  $h_a$ , compared with other substances used mainly for this purpose, typically liquid primary HTFs. The wall over-temperature is significant, especially when the concentrated heat flux absorbed  $\dot{q}_u$  is high. As a consequence, the risk of receiver overheating arises, as long as air temperature  $T$  grows toward the outlet of the receiver tube. The low specific heat capacity of air (half of steam and one-quarter of liquid water) requires high mass flow rates to control the temperature at the receiver outlet. As much as the incoming solar power grows, for high irradiance of large concentrating surfaces, the mass flow should increase, which mainly turns

into high flow velocities, due to low air densities. As a consequence, the pumping power needed to drive air across the receiver could be very high, even in the same order of magnitude as solar power. The authors proposed the innovative T-SAH, which can minimize these limitations. Compressing air at the receiver entrance increases its density and reduces its velocity as well as the pressure drop across the solar field, whereas a turbine installed at the outlet recovers the compression power through the air expansion. In a well-designed system, the turbine can provide all the power required for compressing and pumping, thus avoiding external auxiliary energy consumption. This layout corresponds to an open circuit Brayton cycle of null mechanical efficiency, whose main goal is to provide a hot airflow, instead of providing mechanical power at the shaft. Although losing part of its enthalpy through the expansion, air outgoing the turbine at medium temperature in the range of 300 °C–400 °C, it is available for the user's thermal process. A commercial turbocharger, originally developed to improve automotive engine performances, is used for the purpose, being the compressor and the turbine joined by a shared free-wheeling shaft in a compact and reliable device. Either LFCs or PTCs can be used as solar concentration technology.

In the present study, LFCs are used to implement the above mentioned T-SAH concept, according to the layout in Fig. 1. Despite they still are in the early stage of their application, LFCs have some advantages over PTCs. The segmented primary reflector, Fig. 2 requires a simpler tracking system since the mirrors are smaller and they rotate close to the ground. For the same reason, wind load and visibility are lower with LFCs than with PTCs. While in many PTC systems the receiver moves during tracking, it is fixed in LFCs, allowing a stationary connection with the circuit. This is especially beneficial in the present layout since flexible connections would introduce additional undesired frictional pressure drops. Although the optical efficiency of LFC is lower compared with PTC, LFCs offer the potential of cost-reduction [14]. In Fig. 1 a simple U-loop with two LFCs rows is shown as an example. Compressor *c* and turbine *e* installed at solar receiver inlet and outlet respectively are joined as in a turbocharger. The auxiliary compressor *ac* is required for the starting transient and control purposes. It would be off while the system operates normally. In the following section a numerical model of the T-SAH concept, based on commercial LFCs and turbochargers, is described. The quasi-steady approximation is here used.

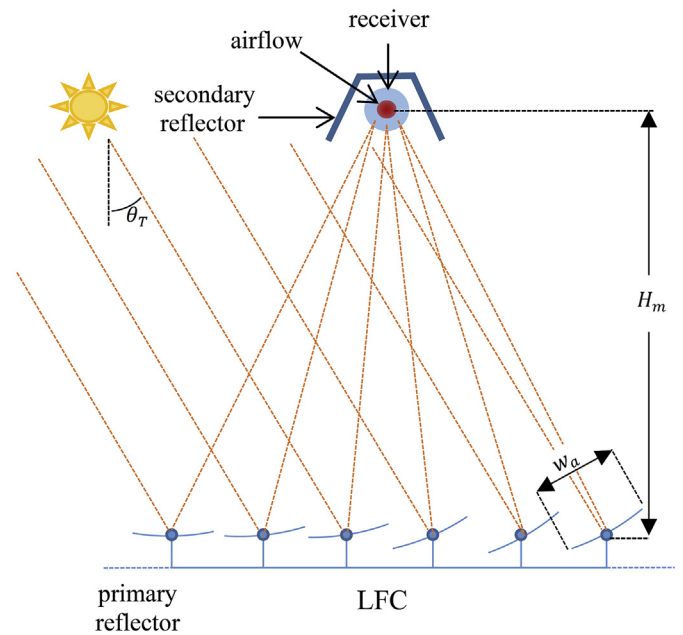


Fig. 2. LFC scheme with primary and secondary reflector, air flowing inside the evacuated tube receiver.

### 2.1. Solar field

The Turbo-assisted Solar Air Heater T-SAH admits a variety of configurations, combining several LFC modules in series and parallel layouts, connected to a single turbocharger to reach the required temperature and mass flow rate. Fig. 1 shows a single U-loop scheme, which can incorporate a series of  $n_s$  LFC modules of length  $L_m$  each, forming two parallel collector rows of equal length  $L_{row} = L_m n_s / 2$ , thus scaling up. Thermally isolated piping elements connect the two rows to the turbocharger unit and between them, with length  $L_{n1}$ ,  $L_{n2}$  and  $L_{n3}$ . The flow leaving the compressor, point (2), enters the U-loop to be heated before entering the turbine (3).  $n_p$  U-loops are connected in parallel to the turbocharger unit, reaching an overall solar field area of  $A_{tot} = 633.6\text{m}^2$ . Geometrical symmetry obtained placing the turbo unit at the center of the plant enables to consider equal U-loops, so that the mass flow rate  $\dot{m}$

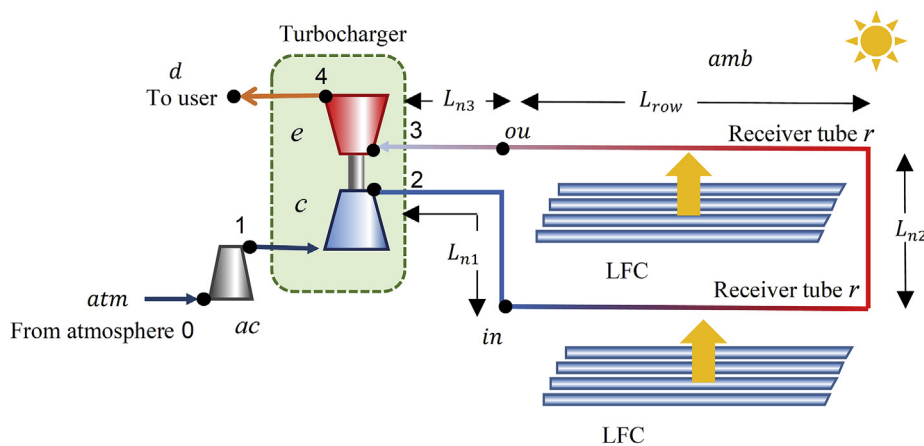


Fig. 1. Turbo-assisted solar air heater T-SAH layout using LFC with  $n_s = 2$  and  $n_p = 1$ .

**Table 2**  
Coefficients of the  $U_L$  correlation in Eq. (6).

$U_L$ coefficients		
$c_{U0}$	$-5.075 \cdot 10^{-3}$	$W m^{-2} K^{-1}$
$c_{U1}$	0.011	$W m^{-2} K^{-2}$
$c_{U2}$	$-3.076 \cdot 10^{-5}$	$W m^{-2} K^{-3}$
$c_{U3}$	$7.645 \cdot 10^{-8}$	$W m^{-2} K^{-4}$

flowing through the turbocharger is equally split into  $n_p$  flows. Table 4 summarizes the main parameters used for setting a solar field for a small industrial facility, incorporating current off-the-shelf technology.

2.1.1. Linear Fresnel collector

A linear Fresnel collector concentrates the solar irradiance received on the aperture area of  $n_m$  parallel mirrors each of aperture  $w_a$ , towards the receiver tube, Fig. 2, having an external perimeter  $P_{ex} = D_{ex}\pi$ . The concentrated irradiance  $\dot{q}_s = \eta_{op}G_{bn}W_a/P_{ex}$  results from normal direct solar irradiance  $G_{bn}$  received by the overall aperture width  $W_a = n_m w_a$  through an optical efficiency  $\eta_{op}$ , which depends on the collector geometry and manufacturing accuracy, as well as on the sun position, collector orientation, and location, [14].

The sun incidence angle on the collector area can be expressed using two components, a longitudinal one  $\theta_L$  and a transversal one  $\theta_T$ , which are the projections of the solar ray on the vertical planes, respectively perpendicular and parallel to the receiver axis. A longitudinal incidence angle  $\theta_i$  is defined as the angle between the solar beam and its projection on the transversal plane. Several authors use  $\theta_i$  instead of  $\theta_L$  to characterize the longitudinal angle-dependent variables [15], Fig. 3. They can be obtained from the collector azimuth angle  $\gamma_r$  and the sun position, i.e. sun azimuth  $\gamma_s$  and elevation  $\alpha_s$  angles [16], and [17], Eqs. (1)–(3).

$$\theta_L = \tan^{-1} \left[ \cos(\gamma_s - \gamma_r) \tan\left(\frac{\pi}{2} - \alpha_s\right) \right] \quad (1)$$

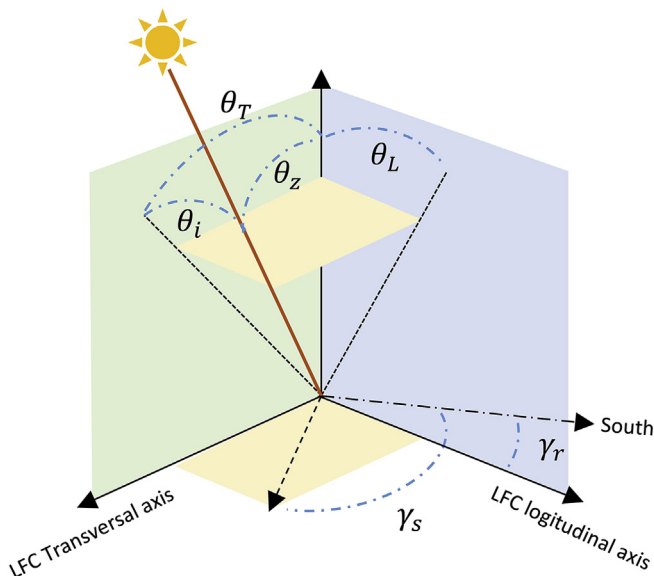


Fig. 3. LFC angles.

$$\theta_T = \tan^{-1} \left[ |\sin(\gamma_s - \gamma_r)| \tan\left(\frac{\pi}{2} - \alpha_s\right) \right] \quad (2)$$

$$\theta_i = \sin^{-1} \left[ \cos(\gamma_s - \gamma_r) \sin\left(\frac{\pi}{2} - \alpha_s\right) \right] \quad (3)$$

A common approach used to determine the effect of the incidence on the optical efficiency  $\eta_{op}$  involves the definition of a peak optical efficiency  $\eta_{op0}$  and an Incident Angle Modifier  $IAM(\theta_i, \theta_T)$ , where herewith indicates functional dependence.  $\eta_{op0}$  is the optical efficiency at normal incidence, thus corresponding  $\theta_i = \theta_T = 0$  deg. The  $IAM$  accounts for the reduction of  $\eta_{op}$  due to incidence angle: cosine effect, produced by a non-null incident angle of sun rays with respect to the reflecting surface normal direction, mutual shadowing, blocking, anisotropic mirrors properties variation, secondary optics optical efficiency variation, and its shadowing effect on the reflectors. Factorization is commonly accepted to express  $IAM$  as the product of the transversal and the longitudinal components  $IAM(\theta_i, \theta_T) = IAM_L(\theta_i)IAM_T(\theta_T)$ . The concentrated irradiance  $\dot{q}_s$  results as in Eq. (4).

$$\dot{q}_s = G_{bn}IAM_T(\theta_T)IAM_L(\theta_i)\eta_{op0}\frac{W_a}{P_{ex}} \quad (4)$$

$\eta_{op0}$  and  $IAMs$  can be obtained either applying raytracing techniques or from measurement campaigns and are generally provided by the manufacturer. The main parameters describing the LFC module selected for the present analysis [18], are reported in Table 4. Fig. 4 shows the  $IAM_L$  and  $IAM_T$  of the selected LFC.  $IAM_L$  does not include optical end losses.

2.1.2. Optical end losses

For non-null longitudinal incidence angles, the concentrated solar irradiance can impact away from the tube end, while at the opposite receiver end, some length is not illuminated. This effect, referred to as end losses, is another angle-dependent optical loss. Although some authors include end losses into  $IAM$ , here they are

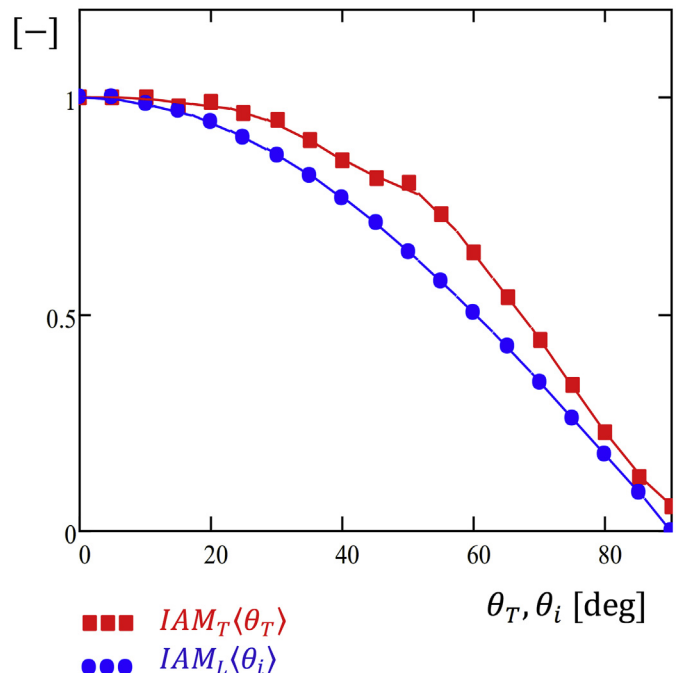


Fig. 4.  $IAM_T$  and  $IAM_L$  of the selected LFC.

evaluated separately accounted by a factor  $f_{end}$ , [19]. To estimate their impact on the LFC performances, which is especially critical for relatively short rows, typical in small and medium scale installations [20], offers its study. Here, for the whole row, the length of the receiver tube is considered equal to the mirror field length and just above it.

Each one of the  $n_m$  mirrors produce slightly different non-illuminated tail length due to the variation of their distance from the receiver. A global mean factor can be defined considering an average distance  $\bar{H}_m$  [15]:

$$f_{end} = 1 - \frac{\bar{H}_m \tan|\theta_i|}{L_{row}}; \bar{H}_m = \sqrt{\left(\frac{W_a}{4}\right)^2 + H_m^2} \quad (5)$$

The portion of receiver length effectively impacted by solar heat flux  $\dot{q}_s$  (Eq. (4)) is estimated as  $L = L_{row}f_{end}$ . The residual length that is non-illuminated  $(1 - f_{end})L_{row}$  receives  $\dot{q}_s = 0$ .

### 2.1.3. Evacuated receiver tube

High-performance commercial receivers minimize thermal losses to the ambient. A selective coating reduces infrared radiation to ambient. Evacuated glass cover reduces the thermal convection losses. A global heat transfer coefficient  $U_L$  controls the combined heat transfer from the external tube surface to ambient through the coaxial glass tube. A physical model to predict  $U_L$ , considering the heat transfer mechanisms involved and material thermal properties was presented by Ref. [21], among others. Burkholder et al. [22] reported thermal losses from a measurement campaign on an evacuated tube receiver. A polynomial correlation for  $U_L(T_w, T_{amb})$  can be obtained from their data, for an evacuated tubes having  $D_{ex} = 0.070$  m, surrounded by an ambient temperature  $T_{amb} = 23^\circ\text{C}$ , Eq. (6), with the resulting coefficients in Table 2. Fig. 5 shows the resulting least-squares fit.

$$U_L(T_w, T_{amb}) = c_{U3}(T_w - T_{amb})^3 + c_{U2}(T_w - T_{amb})^2 + c_{U1}(T_w - T_{amb}) + c_{U0} \quad (6)$$

Wall temperature results from the heat balance at the receiver wall, Eq. (7). Internal heat transfer coefficient  $h_a$  can be estimated using the Dittus-Boelter correlation [23] where the Reynolds

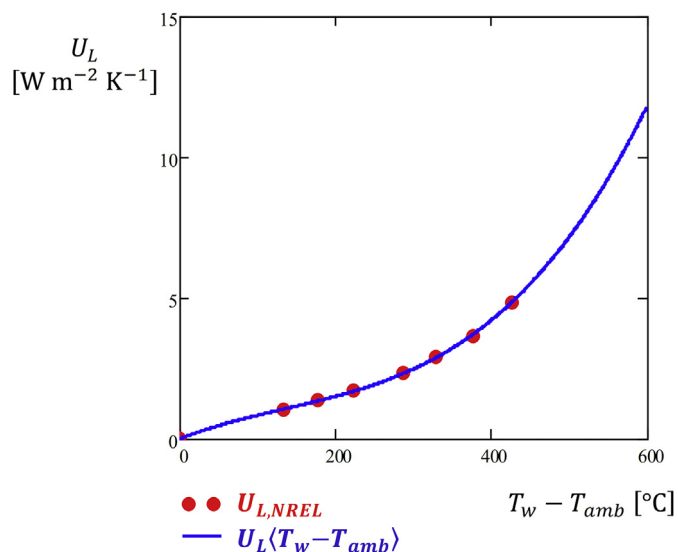


Fig. 5. Correlation for  $U_L(T_w, T_{amb})$  fitting NREL data, according to Eq. (6).

numbers is  $Re_D > 10^4$  and the Prandtl number is  $Pr$ , where  $\dot{m}$  stands for the mass flow rate, Eq. (8).

$$\dot{q}_s - U_L(T_w - T_{amb}) = \dot{q}_u = \frac{h_a P(T_w - T)}{P_{ex}} \quad (7)$$

$$h_a = \frac{k}{D} 0.023 Re_D^{0.8} Pr^{0.4}; Re_D = \frac{4\dot{m}}{\mu\pi D} \quad (8)$$

The approach followed in this study aims at low computation effort, high model flexibility, and accuracy suitable for feasibility analysis. For that reason, the methodology recommended by Ref. [24] seems suitable. Thus, the useful heat power  $\dot{Q}_u$  transferred to the airflow across a certain irradiated receiver length  $L$  can be expressed in terms of inlet temperature  $T_{in}$  and ambient temperature  $T_{amb}$  alone. It relies on constant  $U_L$ ,  $h_a$ ,  $\dot{q}_s$ , and fluid properties, along the considered receiver length  $L$ , with  $t$  indicating stagnation properties.

$$\dot{Q}_u = F_R L P_{ex} \left[ \dot{q}_s - U_L(T_{in} - T_{amb}) \right] = \dot{m}(c_{p,ou} T_{ou,t} - c_{p,in} T_{in,t}) \quad (9)$$

Analytical expressions are possible connecting  $T_w$  and  $T$ , assuming lengthwise constant parameters  $U_L$  and  $h_a$ . Eq. (10) gives the collector efficiency factor  $F'$ , here including  $P_{ex} > P$ . The heat removal factor  $F_R$  is obtained integrating the temperature from the tube inlet  $x = 0$  where  $T = T_{in}$  to the outlet  $x = L$  where  $T = T_{ou}$ , Eq. (11).

$$F' = \frac{\dot{q}_s - U_L(T_w - T_{amb})}{\dot{q}_s - U_L(T - T_{amb})} = \frac{\dot{q}_s - U_L(T_w - T_{amb})}{\dot{q}_s - U_L(T_w - T_{amb}) + U_L \Delta T_w} = \frac{1}{1 + \frac{U_L \Delta T_w}{\dot{q}_s - U_L(T_w - T_{amb})}} = \frac{1}{1 + \frac{U_L P_{ex}}{h_a P}} \quad (10)$$

$$F' P_{ex} dx = \frac{\dot{m} c_p dT_t}{[\dot{q}_s - U_L(T - T_{amb})]} \Rightarrow F_R = \frac{\dot{m} c_p}{L P_{ex} U_L} \left[ 1 - \exp\left(-\frac{L F' P_{ex} U_L}{\dot{m} c_p}\right) \right] \quad (11)$$

Values of  $U_L$ ,  $h_a$  and fluid properties are temperature-dependent variables and can be estimated at the inlet where  $T_{in}$  is known and  $T_{w,in}$  can be estimated iteratively through Eq. (7). Due to considerable temperature variation expected along with the receiver, the row length illuminated  $L_{row}f_{end}$  is discretized into  $n_e$  elements, thus reducing the error associated with constant  $U_L$ ,  $h_a$  and fluid properties assumption. Eqs. (9)–(11) were applied on consecutive elements using  $L = \frac{L_{row}f_{end}}{n_e}$ . A few discretization elements  $n_e = n_s / 2$  were considered enough for the simulation so that  $L \leq L_m$ . Non-irradiated receiver tail has null  $\dot{q}_s$  but still heat losses to ambient. The methodology indicated by Eqs. (9)–(11) is then applied to  $L_{row}(1 - f_{end})$  considering  $\dot{q}_s = 0$ . Due to the modest temperature variation expected across the non-irradiated tail, it is not discretized.

The total pressure drop across a receiver element of length  $L$ ,  $\Delta p_{r,t} = p_{in,t} - p_{ou,t}$  results from the kinetic pressure change  $\Delta p_{k,t}$  due to density variation and the friction pressure drop  $\Delta p_{f,t}$ . Using an average air density  $\rho_m$  at an average temperature and neglecting Mach number correction for being much smaller than unity,  $\Delta p_{r,t}$  results in Eq. (12). The Darcy friction factor  $f$  is modeled using the Blasius formulation of turbulent flow inside smooth tubes, Eq. (13).

$$\Delta p_{r,t} = \underbrace{\Delta p_{k,t}}_{\frac{1}{2}(\rho_{ou}v_{ou}^2 - \rho_{in}v_{in}^2)} + \underbrace{\Delta p_{f,t}}_{\frac{1}{2}\rho_m v^2 \left( f \frac{L}{D} \right)} = \frac{1}{2} \left( \frac{4\dot{m}}{\pi D^2} \right)^2 \left( \frac{1}{\rho_{ou}} - \frac{1}{\rho_{in}} + f \frac{L}{\rho_m D} \right) \quad (12)$$

$$f = 0.316 Re_D^{-1/4} \quad (13)$$

The receiver tube thermal model has been contrasted against the validated theoretical model of [25], one of a few studies on gaseous HTF in concentrating collectors. These authors modeled the 100 m long collector ET-II. The present model gave a difference in the output temperature of -1.75% as reported in Table 3.

### 2.1.4. Connection pipes

Connection pipes required for the U-loop configuration can be modeled using the same equations of the receiver, Eqs. (9)–(11), using  $\dot{q}_s = 0$  and a proper thermal losses coefficient  $U_{Ln}$ , as in Eq. (14).  $U_{Ln}$  depends on the thermal insulation thickness and composition, so that it can be expressed as in Eq. (15).

$$\dot{Q}_u = -F_R L P_{ex} U_{Ln} (T_{in} - T_{amb}) = \dot{m} (c_{p,ou} T_{ou,t} - c_{p,in} T_{in,t}) \quad (14)$$

$$U_{Ln}^{-1} = \frac{\ln \left( \frac{D_{ins}}{D_{n,ex}} \right) D_{n,ex}}{2k_{ins}} + \frac{D_{n,ex}}{D_{ins} h_{amb}} \quad (15)$$

A constant  $U_{Ln} = 1.8 \text{ W m}^{-2} \text{ K}^{-1}$  has been calculated, corresponding to an insulation effective thermal conductivity  $k_{ins} = 0.1 \text{ W m}^{-1} \text{ K}^{-1}$  of mineral rock at the average temperature of  $\sim 330 \text{ }^\circ\text{C}$ , with an insulation external diameter  $D_{ins} = 5D_{n,ex}$ .

Again, the total pressure drop along the connection pipe of length  $L_{ni}$  can be obtained from kinetic and frictional components Eq. (16), including concentrated loss coefficient  $K_{ni} = 2$ , with  $i = 1-3$ , being  $f$  estimated using Eq. (13) on diameter  $D_n$ .

$$\Delta p_{n_i,t} = \underbrace{\Delta p_{k,t}}_{\frac{1}{2}(\rho_{ou}v_{ou}^2 - \rho_{in}v_{in}^2)} + \underbrace{\Delta p_{f,t}}_{\frac{1}{2}\rho_m v^2 \left( f \frac{L_{ni}}{D_n} + K_{ni} \right)} = \frac{1}{2} \left( \frac{4\dot{m}}{\pi D_n^2} \right)^2 \left( \frac{1}{\rho_{ou}} - \frac{1}{\rho_{in}} + f \frac{L_{ni}}{\rho_m D_n} + \frac{K_{ni}}{\rho_m} \right) \quad (16)$$

## 2.2. Turbocharger

Turbochargers were developed by the automotive industry to increase reciprocating engines inlet air density using waste exhaust energy. A centrifugal compressor is driven by the enthalpy and pressure at the inlet of an exhaust turbine, sharing the same shaft and rotating at the rotational speed  $n_T$ . The working principle lays on the fact that the mechanical power provided by the fluid expansion across the turbine  $\dot{W}_e$  is transferred to the compressor

via the common shaft, providing the compressing power  $\dot{W}_c$ . A mechanical efficiency  $\eta_m$  accounts for the mechanical losses at the shaft. The application of Newton's second law of rotating systems to a turbocharger rotor results in Eq. (17), being  $J_T$  the turbocharger polar inertia.

$$\left( \frac{\dot{W}_e \eta_m}{n_T} - \frac{\dot{W}_c}{n_T} \right) \frac{1}{J_T} = 2\pi \frac{dn_T}{dt} \quad (17)$$

Under steady-state free-wheeling rotation, Eq. (17) reduces to Eq. (18), being  $n_T$  constant.

$$\dot{W}_e \eta_m - \dot{W}_c = \dot{W}_{net} = 0 \quad (18)$$

According to cycle points nomenclature in Fig. 1, assuming a process's path perfect gas behavior, the turbomachines power can be estimated from isentropic total to total efficiencies  $\eta_c$  and  $\eta_e$ , pressure ratios  $\pi_c = \frac{p_{2t}}{p_{1t}}$  and  $\pi_e = \frac{p_{3t}}{p_{4t}}$ , and inlet stagnation temperatures  $T_{1t}$  and  $T_{3t}$ , respectively for the compressor Eq. (19) and the turbine Eq. (20), where  $\gamma = c_p/c_v$ .

$$\dot{W}_c = \dot{m}_c c_{p,c} T_{1t} \left( \pi_c^{\frac{\gamma_c-1}{\gamma_c}} - 1 \right) \eta_c^{-1} \quad (19)$$

$$\dot{W}_e = \dot{m}_e c_{p,e} T_{3t} \left[ 1 - \pi_e^{-\frac{\gamma_e-1}{\gamma_e}} \right] \eta_e \quad (20)$$

Outlet total temperatures result from Eq. (21) and Eq. (22).

$$T_{2t} = T_{1t} \left[ 1 + \left( \pi_c^{\frac{\gamma_c-1}{\gamma_c}} - 1 \right) \eta_c^{-1} \right] \quad (21)$$

$$T_{4t} = T_{3t} \left[ 1 - \eta_e \left( 1 - \pi_e^{-\frac{\gamma_e-1}{\gamma_e}} \right) \right] \quad (22)$$

As mentioned, the auxiliary compressor  $ac$  is excluded by the circuit if not specified. When  $ac$  is active, it impacts the compressor inlet conditions,  $p_{1t} = p_{0t} \pi_{ac}$  and  $T_{1t}$ , Eq. (24), consuming the external power  $\dot{W}_{ac}$ , Eq. (23).

$$\dot{W}_{ac} = \dot{m}_c c_{p,c} T_{0t} \left( \pi_{ac}^{\frac{\gamma_{ac}-1}{\gamma_{ac}}} - 1 \right) \eta_{ac}^{-1} \quad (23)$$

$$T_{1t} = T_{0t} \left[ 1 + \left( \pi_{ac}^{\frac{\gamma_{ac}-1}{\gamma_{ac}}} - 1 \right) \eta_{ac}^{-1} \right] \quad (24)$$

Aiming at a OD quasi-steady-state model, functional relations need to correlate pressure ratios  $\pi_c$  and  $\pi_e$ , as well as isentropic efficiencies  $\eta_c$  and  $\eta_e$ , with mass flow rate  $\dot{m}$ , rotational speed  $n_T$ , and inlet temperatures  $T_{1t}$  and  $T_{3t}$ . The following subsections address this topic.

### 2.2.1. Compressor

Two relations  $\pi_c = \pi_c(\dot{m}_c, T_{in}, n_T)$  and  $\eta_c = \eta_c(\dot{m}_c, T_{in}, n_T)$

**Table 3**  
Receiver tube thermal model validation.

Input values				Literature [25]		Present model		Deviation
$\dot{m}$	$\dot{q}_s$	$p_{in}$	$T_{in}$	HTF	$T_{ou}$	HTF	$T_{ou}^{cal}$	$\frac{T_{ou}^{cal} - T_{ou}}{T_{ou} - T_{in}}$
1.1 kg s <sup>-1</sup>	17.71 kW m <sup>-2</sup>	75 bar	225°C	nitrogen	502°C	air	497°C	-1.75 %

describe the compressor performances map. Extrapolation of performance maps provided by the manufacturer gives continuous relations [26]. Corrections are used for entering the map, based on reference inlet temperature and pressure,  $T_{c,ref}$ ,  $p_{c,ref}$ , Eqs. (25) and (26).

$$\dot{m}_{c,cor} = \dot{m}_c \sqrt{\frac{T_{c,in}}{T_{c,ref}}} \frac{p_{c,ref}}{p_{cin}} \quad (25)$$

$$n_{c,cor} = n_T \sqrt{\frac{T_{c,ref}}{T_{cin}}} \quad (26)$$

On the compressor map, the relation  $\pi_c \langle \dot{m}_{c,cor} \rangle$  is plotted for different corrected speeds  $n_{c,cor}$ , providing a set of iso-speed curves. It is common to overlap them with iso-efficiency curves, representing the relation  $\pi_c \langle \dot{m}_{c,cor} \rangle$  for several constant efficiencies  $\eta_c$ , Fig. 6(a).

**2.2.1.1. Pressure ratio fitting function.** Jensen et al. [27] describes the methodology used here for the extrapolation of  $\pi_c = \pi_c \langle \dot{m}_c, T_{in}, n_T \rangle$  from iso-speed curves. It has been applied by Ref. [28] with excellent results, and it was recommended by Ref. [26]. The non-dimensional flow rate parameter  $\varphi_c$  and head parameter  $\psi_c$  are defined through the tip blade speed  $U_c$  and the compressor rotor diameter  $D_c$ . Variables  $c_p, \rho_a, \gamma_c$  are evaluated at the reference temperature  $T_{c,ref}$ .

$$\varphi_c = \frac{\dot{m}_{c,cor}}{\rho_a \frac{\pi}{4} D_c^2 U_c} \quad (27)$$

$$\psi_c = \frac{c_p T_{c,ref} \left( \pi_c^{\frac{\gamma_c-1}{\gamma_c}} - 1 \right)}{U_c^2 / 2} \quad (28)$$

$$U_c = n_{c,cor} \pi D_c \quad (29)$$

The authors proposed to fit a function  $\psi_c \langle \varphi_c, n_{c,cor} \rangle$ , using six parameters  $k_{ij}$  and the inlet Mach number  $Ma$ , which can be determined from iso-speed curves data fitting using the least-squares algorithm. To increase the accuracy, a third-order polynomial form for  $k_i \langle Ma \rangle$  fit is applied, as done by Ref. [29], using nine parameters  $k_{ij}$ , Eq. (31). The function  $\pi_c = \pi_c \langle \dot{m}_c, n_{c,cor} \rangle$  results as in Eq. (32).

$$Ma = \frac{U_c}{\sqrt{\gamma_c R T_{c,ref}}} \quad (30)$$

$$\psi_c = \frac{k_1 + k_2 \varphi_c}{k_3 - \varphi_c}; \quad k_i = k_{i1} + k_{i2} Ma + k_{i3} Ma^2 \quad (31)$$

From Eqs. (28) and (29):

$$\pi_c = \left[ \frac{\frac{1}{2} (n_{c,cor} \pi D_c)^2 \psi_c \varphi_c \dot{m}_{c,cor}, n_{c,cor}, n_{c,cor}}{c_p T_{c,ref}} + 1 \right]^{\gamma_c / (\gamma_c - 1)} \quad (32)$$

Fig. 6(a) shows the modeled  $\pi_c \langle \dot{m}_{c,cor}, n_{c,cor} \rangle$  of a representative compressor map for comparison with experimental data.

**2.2.1.2. Efficiency fitting function.** The compressor map gives two alternative types of curves: a) iso-efficiency curves  $\eta_c \langle \dot{m}_{c,cor}, \pi_c \rangle =$

const. or b) iso-speed efficiency curves  $\eta_c \langle \dot{m}_{c,cor}, n_{c,cor} \rangle = \text{const.}$ , Fig. 6(a). Although the technical literature offered both approaches, the second one gives better results for the present case. An extrapolation method was presented by Ref. [27], analogous to the mass flow fitting, as well as by Refs. [29,30]. Galindo et al. [31,32] offered more complex procedures aiming at higher accuracy. This paper offers an original method based on a local interpolation, keeping a low computational load. It relies on recognizing that on one side of the dorsal line of maximum efficiency  $\eta_{c,max}$ , Fig. 6(a), the compressor behavior is different. On the left side the surge phenomenon appears while at the right side, sonic choke appears.

First, each iso-speed  $\eta_c \langle \dot{m}_{c,cor}, n_{c,cor} \rangle = \text{const.}$  data from the map were normalized to obtain the normalized efficiency  $\eta_{c,norm} \langle \varphi_{c,norm} \rangle$  using a normalized non-dimensional mass flow rate  $\varphi_{c,norm}$ , Eq. (34), following the normalization adopted by Ref. [31]. Each iso-speed efficiency data set is normalized with the maximum efficiency at such speed  $\eta_{c,max}$  at the dorsal line. The non-dimensional mass flow  $\varphi_c$  is defined in Eq. (27) and is normalized using  $\varphi_{c,max}$ , which is calculated from  $\dot{m}_{c,cor}^{max}$ , the abscissa of the dorsal line in the map.

$$\eta_{c,norm} = \frac{\eta_c}{\eta_{c,max}} \quad (33)$$

$$\varphi_{c,norm} = \frac{\varphi_c}{\varphi_{c,max}} \quad (34)$$

Second-order polynomial regression is applied to each normalized iso-speed data set, separately for the two regions at both sides of the dorsal line  $\varphi_{c,norm} < 1$  and  $\varphi_{c,norm} > 1$  with the result of high accuracy, Fig. 6(c). Once the functions  $\eta_{c,norm} = f_{n,i} \langle \varphi_{c,norm} \rangle$  are obtained, an interpolation ratio  $IR$  determines  $\eta_{c,norm}$  for a generic  $\varphi_{c,norm}$  and speed  $n_{c,corI} < n_{c,cor} < n_{c,corII}$ , Eqs. (35) and (36).

$$\eta_{c,norm} = f_{n,I} \varphi_{c,norm} (1 - IR) + f_{n,II} \varphi_{c,norm} IR \quad (35)$$

$$IR = \frac{n_{c,cor} - n_{c,corI}}{n_{c,corII} - n_{c,corI}} \quad (36)$$

The functions for  $\varphi_{c,max} \langle n_{c,cor} \rangle$  and  $\eta_{c,max} \langle n_{c,cor} \rangle$  were obtained applying the respective polynomial regressions on the values from the map. Only the monotonically increasing interval of  $f_{n,i} \langle \varphi_{c,norm} \rangle$  was considered for the left region and  $\varphi_{c,norm} < 1$  and only monotonically decreasing interval of  $f_{n,i} \langle \varphi_{c,norm} \rangle$  was considered for the right region  $\varphi_{c,norm} > 1$ .  $\eta_{c,norm} = 1$  was imposed to ensure continuity between the left and right regions functions around  $\varphi_{c,norm} = 1$ . Fig. 6 shows the results.

### 2.2.2. Turbine

Several authors presented methodologies for turbine flow map extrapolation [33,34], and [35], among others. They are applicable when the turbine map provided by the manufacturer reports the function  $\dot{m}_e \langle \pi_e, n_T \rangle$  at constant speed for several speed values. However, in most cases, only one curve is provided, approximating the iso-speed mass flow curves. Corrected values are customary, as for the compressor, Eqs. (37) and (38).

$$\dot{m}_{e,cor} = \frac{p_{e,ref}}{p_{e,in}} \sqrt{\frac{T_{e,in}}{T_{e,ref}}} \dot{m}_e \quad (37)$$

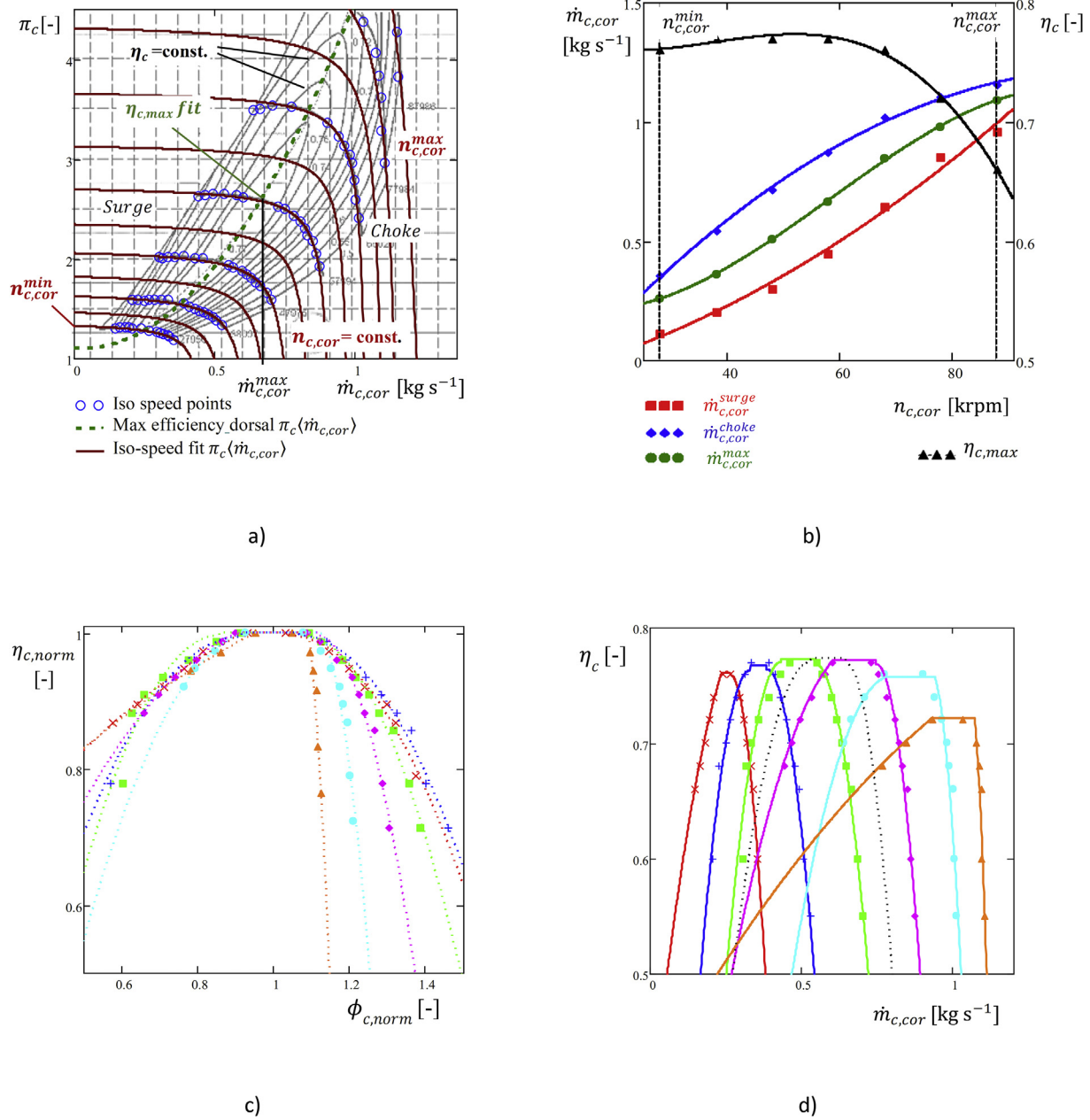


**Fig. 6.** Compressor model results superimposed to data dots. a) Compressor map with superposed  $\pi_c(\dot{m}_{c,cor})$  for  $n_{c,cor} = const.$  (blue circle dots and brown line) and maximum efficiency dorsal line  $\pi_c(\dot{m}_{c,cor})$  (green dash), b) Choke and surge limits, dorsal-speed lines  $\eta_{c,max}(n_{c,cor})$  and  $\dot{m}_{c,cor}(n_{c,cor})$ . c) normalized iso-speed efficiency curves. d) iso-speed efficiency  $\eta_c(\dot{m}_{c,cor})$ .  $T_{e,ref} = 302.6 K$ ;  $p_{c,ref} = 0.962 bar$ ;  $D_c = 133 mm$ . (For interpretation of the references to colour in this figure legend, the reader is referred to the Web version of this article.)

$$n_{e,corr} = n_T \sqrt{\frac{T_{e,ref}}{T_{e,in}}} \quad (38)$$

Following [26] the relation  $\dot{m}_e(\pi_e)$ , which does not include the speed variable anymore, can be approximated with the function in Eq. (39), with  $c_e$  and  $k_e$  determined by curve fitting.  $T_{e,ref}$  and  $p_{e,ref}$  are given by the manufacturer.

$$\dot{m}_{e,cor} = c_e \sqrt{1 - \pi_e^{k_e}} \quad (39)$$

In most cases, the manufacturers do not provide turbine efficiency curves but only provide a value for maximum efficiency

$\eta_{e,max}$ . Thus, a model is needed for its prediction. Ref. [26] as well as [28] indicated the following model based on turbine blade speed ratio  $SR$ , being the turbine efficiency mainly dependent on the flowing gas angle of incidence to the blades, Eqs. (40)–(42). A tip blade speed  $U_e$  is defined using the turbine wheel diameter  $D_e$ .  $SR_{opt} = 0.7$  as recommended by Ref. [26] as well as elsewhere is used herewith.

$$U_e = D_e \pi n_{e,cor} \quad (40)$$

$$SR\langle n_{e,cor}, \pi_e \rangle = \frac{U_e}{\sqrt{2C_{p,e}T_{e,ref}\left(1 - \pi_e^{\frac{1-\gamma_e}{\gamma_e}}\right)}} \quad (41)$$

$$\eta_e\langle n_{e,cor}, \pi_e \rangle = \eta_{e,max} \left[ \frac{2SR}{SR_{opt}} - \left( \frac{SR}{SR_{opt}} \right)^2 \right] \quad (42)$$

Fig. 7 shows the curves of  $\dot{m}_e\langle \pi_e \rangle$  and  $\eta_e\langle n_{e,cor}, \pi_e \rangle$  that were obtained, according to the model.

### 2.3. Turbo-solar field matching procedure

According to the proposed concept, a few physical constraints define the domain of working conditions for the T-SAHA: I) turbocharger working range, II) the thermal limit of the solar receiver tube and III) the turbocharger freewheeling operation. They are explained as follows.

I) The mass flow rate  $\dot{m} = \dot{m}_c = \dot{m}_e$  and speed  $n_T$  must be within the turbocharger working limits. The allowed  $n_T$  range is defined by its minimum and maximum  $n_{c,cor}$  values, indicated by the compressor map. A range for  $\dot{m}$  is defined for any speed  $n_T$  by the compressor surge and choke limits, indicated on the map, Fig. 6(a–b).

$$n_{c,cor}^{min} < n_{c,cor} < n_{c,cor}^{max} \quad (43)$$

$$\dot{m}_{c,cor}^{surge}\langle n_{c,cor} \rangle < \dot{m}_{c,cor}\langle n_{c,cor} \rangle < \dot{m}_{c,cor}^{choke}\langle n_{c,cor} \rangle \quad (44)$$

II) The receiver thermal limit, Eq. (45), imposes the second constraint. The highest wall temperature takes place at the U-loop outlet (3) in Fig. (1),  $T_{w3}$ , which must be lower than  $T_{w,max}$ .  $T_{w3}$  is affected by  $\dot{q}_s$  and U-loop outlet air temperature  $T_3$ , as well as by  $\dot{m}$ , which determines  $h_a$ . Eq. (7) can be

rewritten and iteratively solved to compute  $T_{w3}$  as in Eq. (45), where  $U_L\langle T_w, T_{amb} \rangle$  is a temperature-dependent variable.

$$T_{w3} = \frac{\dot{q}_s D_{ex} + T_3 D_{ha} + T_{amb} D_{ex} U_L}{D_{ha} + D_{ex} U_L} \leq T_{w,max} \quad (45)$$

III) When Eq. (18) is verified the turbine fully drives the compressor and the turbocharger is freewheeling at constant rotational speed, enabling the T-SAHA to deliver hot air without any external auxiliary pumping power consumption.

According to these three constraints, a suitable turbocharger can be selected considering the solar field parameters and the expected solar and ambient inputs for the specific location, before performing a detailed simulation of T-SAHA behavior.

For a given turbocharger, the simultaneous fulfilment of constraints I, II, and III can be predicted by building a matching map as in Fig. 8. With this aim, the broad range of working conditions corresponding to variable solar and ambient inputs,  $G_{bn}, \gamma_s, \alpha_s, T_{amb}, p_{amb}$ , is approximated considering a concentrated solar irradiance  $\dot{q}_s$  variation in the range  $0 < \dot{q}_s < \dot{q}_{s,peak}$  and assuming  $f_{end} = 1$ ,  $T_{amb} = 15^\circ\text{C}$  and  $p_{amb} = 1.013$  bar for simplicity.  $\dot{q}_{s,peak}$  is the maximum concentrated irradiance expected during the typical year for the selected location. The T-SAHA model described in Sections 2.1–2.2 is then solved for several compressor speed values  $n_{c,cor}$  within the range of expected concentrated solar irradiance  $0 < \dot{q}_s < \dot{q}_{s,peak}$ . A matching map is obtained reporting the theoretical turbocharger excess power  $\dot{W}_{net}$ , for the T-SAHA operating at a constant speed  $n_{c,cor}$ , fulfilling conditions I and II. Fig. 8 indicates one of the best matches obtained according to the solar field parameters reported in Table 4.

$\dot{W}_{net}$  is reported as a percentage of solar power  $\dot{Q}_s = \dot{q}_s P_{ex} 2L_{row} n_p$  against a load factor  $LF = \dot{q}_s / \dot{q}_{s,peak}$ . In a broad range of  $LF$ ,  $\dot{W}_{net}$  can be null choosing a proper speed for a given  $\dot{q}_s$ . This indicates that steady-state freewheeling can be obtained across a large portion of the expected concentrated irradiance

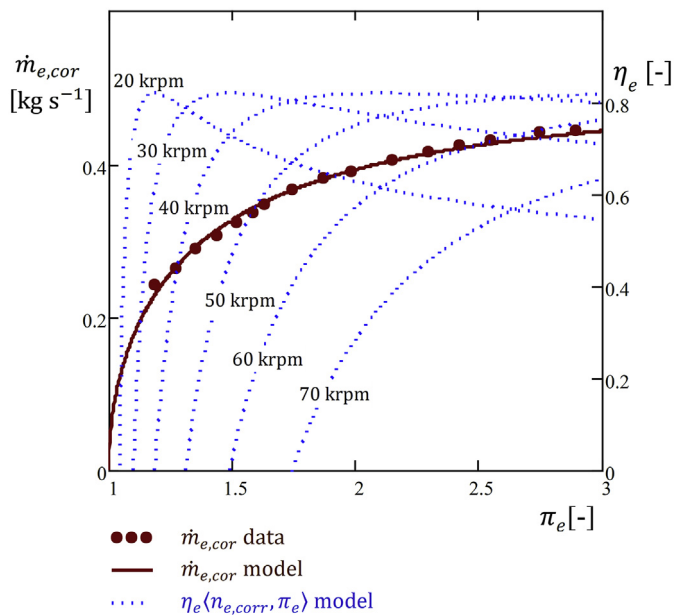


Fig. 7. Turbine results. Turbine data with model superimposed and efficiency map estimation for the fixed geometry turbine.  $T_{e,ref} = 288.8$  K;  $p_{e,ref} = 1.013$  bar;  $D_e = 111.5$  mm;  $\eta_{e,max} = 0.82$ .

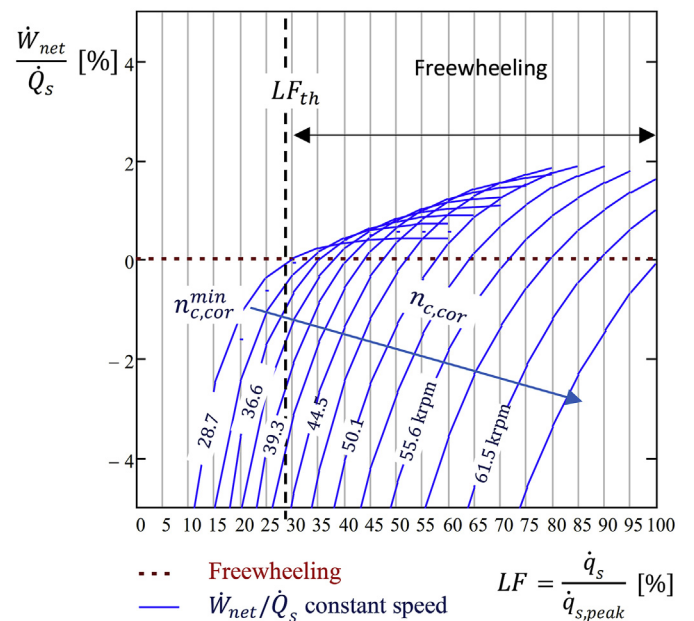


Fig. 8. Matching map.  $\dot{W}_{net}/\dot{Q}_s$  vs.  $LF$  for operating points fulfilling conditions I and II, in Madrid (Spain).

**Table 4**  
Solar field layout, LFC and receiver parameters.

Number of Loops	$n_p$	4
Loop length	$L_{loop}$	52.2 m
Row length	$L_r$	$\frac{L_m n_s}{2} = 15.8$ m
Connections	$L_{n1}$	$W_a \frac{3}{2} + H_m$
	$L_{n2}$	$W_a$
	$L_{n3}$	$\frac{W_a}{2} + H_m$
Connection pipe diameter	$D_n$	0.08 m
Modules per loop	$n_s$	6
Total Active area	$A_{tot}$	633.6 m <sup>2</sup>
Orientation N-S	$\gamma_r$	0°
Module length	$L_m$	5.28 m
Aperture width	$W_a$	5.00 m
Height above mirrors	$H_m$	2.72 m
Module active area	$A_m$	26.40 m <sup>2</sup>
Peak optical efficiency	$\eta_{op0}$	0.632
Number of mirrors per module	$n_m$	10
Mirror aperture	$w_a$	0.50 m
Inner receiver diameter	$D$	0.066 m
Outer receiver diameter	$D_{ex}$	0.07 m

range, excluding very low irradiances. An approximated minimum threshold for the load factor is identified  $LF_{th}$ , defining the low power working limit for the T-SAH to operate correctly. For the settings defined in Table 4 and the location of Madrid (Spain), located at (40° 24' 59" N, 3° 42' 9" W), it results  $LF_{th} \approx 0.3$  with a  $\dot{q}_{s,peak} = 13.5$  kW m<sup>-2</sup>. At low irradiances  $LF < LF_{th}$ , to reach a high enough inlet temperature at the turbine which can then provide the required power, the T-SAH would require a mass flow rate lower than the minimum value allowed by turbocharger constraint I. The turbocharger allows reducing the mass flow rate by decreasing the speed or shifting its working point toward surge, respectively limited by the minimum speed  $n_{c,cor}^{min}$  and the surge limit  $\dot{m}_{c,cor}^{surge}$ , Fig. 6(a–b). In addition, at low speed, the turbocharger efficiencies are lower, impeding to achieve freewheeling. For these reasons, when  $LF < LF_{th}$ , the T-SAH should be shut-down or bypassed. Alternative solutions can be studied to ensure hot air production at marginal load. Although an exhaustive screening of these possibilities is not in the scope of this work, a solution is proposed in Section 3.3.

### 3. Results

In order to evaluate the availability of a T-SAH plant under off-design performances, the numerical model presented in Section 2 is solved with realistic ambient and solar input parameters. A typical meteorological year TMY is used to model  $G_{bn}$ ,  $T_{amb}$ ,  $p_{amb}$  for the specific location selected, according to the current practice in solar thermal engineering [36]. A TMY is built from solar and ambient data measured during several years at a specified location and merged into a single year. The data are reported with a time interval of 1 h. The TMY for Madrid (Spain) (40° 24' 59" N, 3° 42' 9" W), selected as the location, was taken from Ref. [37]. Sun azimuth and elevation,  $\gamma_s$ ,  $\alpha_s$ , for the corresponding hour of the year were computed using the relations in the Appendix. The main T-SAH output are reported and discussed for a representative summer and winter days, as well as for the whole TMY considering the system operating only when the turbocharger freewheeling is achieved, according to the physical constraints detailed in Section 2.3.

#### 3.1. Representative days

Fig. 9 reports the instantaneous results of a representative summer clear day, as a function of the true solar time TST. The direct normal irradiance  $G_{bn}$ , together with IAMs and end losses factor  $f_{end}$  are shown in Fig. 9(a). Despite the relatively short collector length,  $f_{end} > 0.9$  is obtained, according to  $\theta_i$ , Eq. (5). Fig. 9(b) shows the daily variation of thermal power available, lost, and delivered to the user. The hot air delivered at the turbine outlet, holding  $T_a = T_4$ , corresponds to an outlet power  $\dot{Q}_a$ , Eq. (46). The solar power  $\dot{Q}_{bn}$  available on a surface normal to sunrays equivalent to the overall capturing surface  $A_{tot} = A_m n_s n_p$  is evaluated as a reference, Eq. (47). The solar power concentrated on the receiver focal line  $\dot{Q}_s$  varies according to  $G_{bn}$ , optical efficiency and IAMs, Eq. (48).  $\dot{Q}_s$  is not entirely available for the receiver since a portion  $\dot{Q}_{fend} = \dot{Q}_s - \dot{Q}_r$  is lost due to optical end losses, which is relatively low, corresponding to less than 10% of the delivered thermal power  $\dot{Q}_a$ .  $\dot{Q}_r$  represents the solar power that effectively reaches the receiver tube, Eq. (49). Due to thermal losses to the ambient from the receiver surface, as well as from insulated piping, part of the power  $\dot{Q}_r$  is lost. Thermal losses  $\dot{Q}_L = \dot{Q}_r - \dot{Q}_a$  corresponds to around 30% of delivered thermal power  $\dot{Q}_a$ .

$$\dot{Q}_a = (T_{4t} c_{p,4} - T_{amb} c_{p,amb}) \dot{m} \quad (46)$$

$$\dot{Q}_{bn} = G_{bn} A_m n_s n_p \quad (47)$$

$$\dot{Q}_s = G_{bn} \eta_{op0} IAM_T IAM_L A_m n_s n_p \quad (48)$$

$$\dot{Q}_r = G_{bn} \eta_{op0} IAM_T IAM_L f_{end} A_m n_s n_p \quad (49)$$

The operating conditions of the turbocharger and its effect on the air flow and solar receiver tube can be analyzed considering Fig. 9(c)–(d). Fig. 9(c) depicts the air temperature in the main points of the circuit, according to Fig. 1. At the compressor outlet  $T_2$  varies between 100°C and 150°C because of  $\pi_c$ , according to Eq. (21).  $T_3$  reaches a peak of 500°C at midday, whereas the temperature difference  $\Delta T = T_3 - T_2$  across the solar field is quite steady around 350°C, since the mass flow rate  $\dot{m}$ , also reported in Fig. 9(c), increases in concert to the solar power. The increase in U-loop pressure drop  $\Delta p_{m,t} = p_{2t} - p_{3t}$  induced by the higher  $\dot{m}$  when at power peak is moderate thanks to the higher  $\pi_c$ , which leads to higher air densities and lower airflow velocities. Besides, the  $\Delta p_{m,t}$  moderate increase is more than compensated by the higher turbine inlet temperature, resulting in a turbine power increase. This beneficial effect of self-regulation comes from the turbocharger performance map and the good matching of the turbocharger chosen with the solar field. Although the working conditions vary remarkably with solar power, the delivered air temperature  $T_a = T_{4t}$  shows a flat time-profile, varying between 350°C and 380°C.

Concerning the receiver thermal limit, the maximum wall temperature reached by the receiver tube is  $T_{w3} < T_{w,max} = 600$  °C, confirming that the constraint II) formulated in Section 2.3 is respected, Fig. 9(c). The turbocharger performance can be deduced from the main parameter plotted in Fig. 9(d). It works at high compressor and turbine efficiencies  $\eta_c \approx 0.78$  and  $\eta_e \approx 0.80$  almost constantly during the operating hours, while  $\pi_c$ , as well as  $\pi_e$ , varies according to the mass flow rate and irradiance. The corrected compressor speed  $n_{c,cor}$  varies within the allowed limits, Eq. (43), from 40% to 70% of its maximum  $n_{c,cor}^{max}$ .

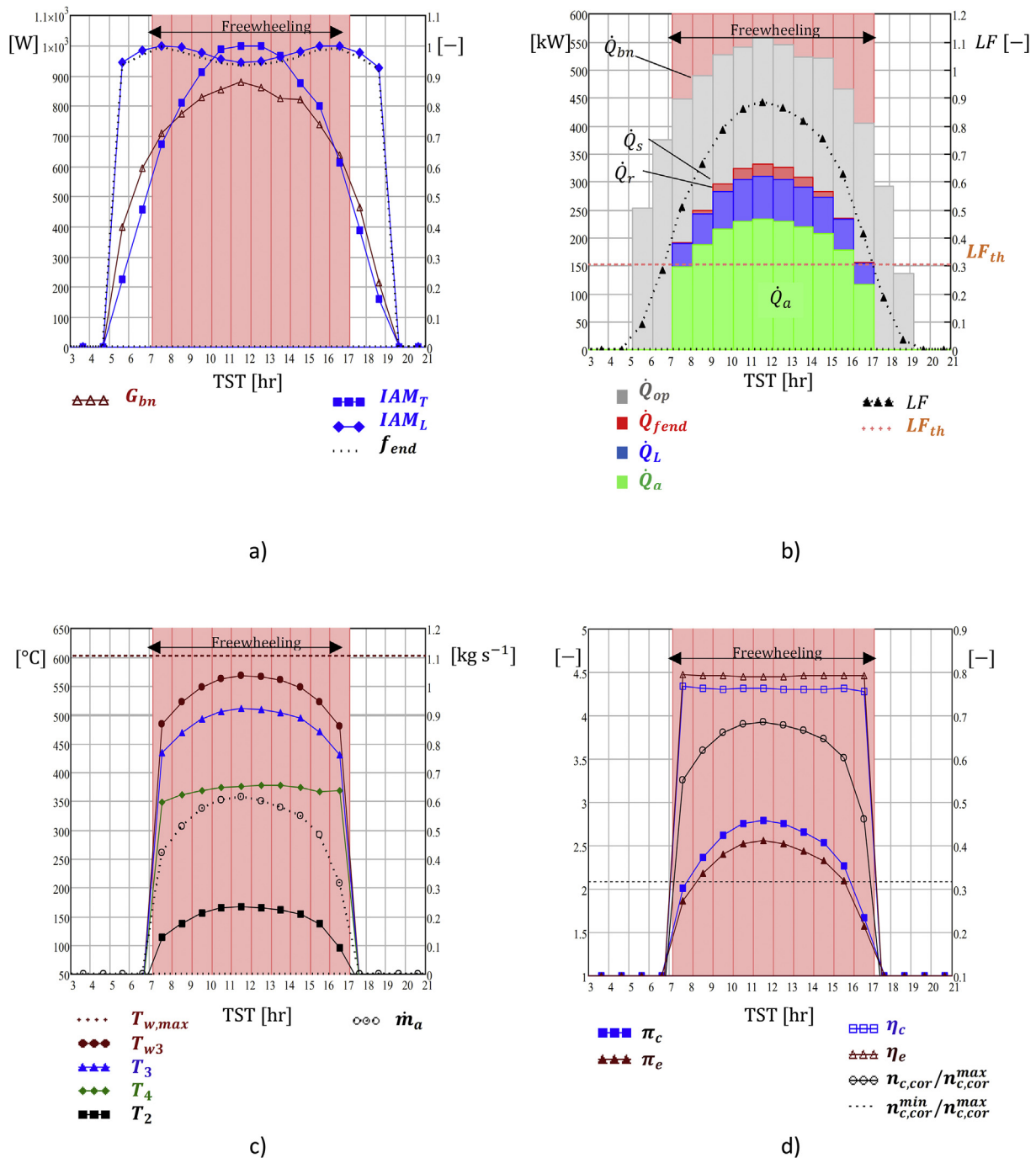


Fig. 9. T-SAHA performances vs. true solar time TST during a clear summer day, Madrid (Spain).

The simulation demonstrated that the T-SAHA operates almost during all daylight time, confirming the excellent turbocharger matching with the solar field performance and the feasibility of the proposed layout on a summer clear day. Only in the early morning and late afternoon hours, turbocharger freewheeling is not achievable and the T-SAHA stops (OFF), as if being the  $LF < LF_{th}$ , Fig. 9(b), confirming the prediction discussed in Section 2.3. The T-SAHA operates for 10 h, over the 14 h of daylight when  $G_{bn} > 0$ . Fig. 9 highlights the hours of freewheeling operation.

The simulation was repeated on a representative winter day with a clear sky. Fig. 10 shows the main results obtained. When comparing them with the results from the summer day-case

discussed above, the optical collector efficiency is lower on the winter day due to a lower  $IAM_L$  because of the higher  $\theta_i$ . This has also a remarkable impact on  $f_{end}$ , which dropped to 0.6 at midday. Optical end losses are relatively higher than in summer day-case, being around 30% of the delivered power  $\dot{Q}_a$ . Higher optical losses translate into a lower concentrated solar power  $\dot{Q}_s$  and  $\dot{Q}_r$ . In contrast, the thermal losses are reduced from summer to winter, as can be seen in Fig. 10(b), due to the lower mean wall temperature reached. On the winter day, the thermal power delivered to the user drops below 100 kW. The operating hours are reduced according to the shorter winter daylight, whereas the low irradiance cut-off

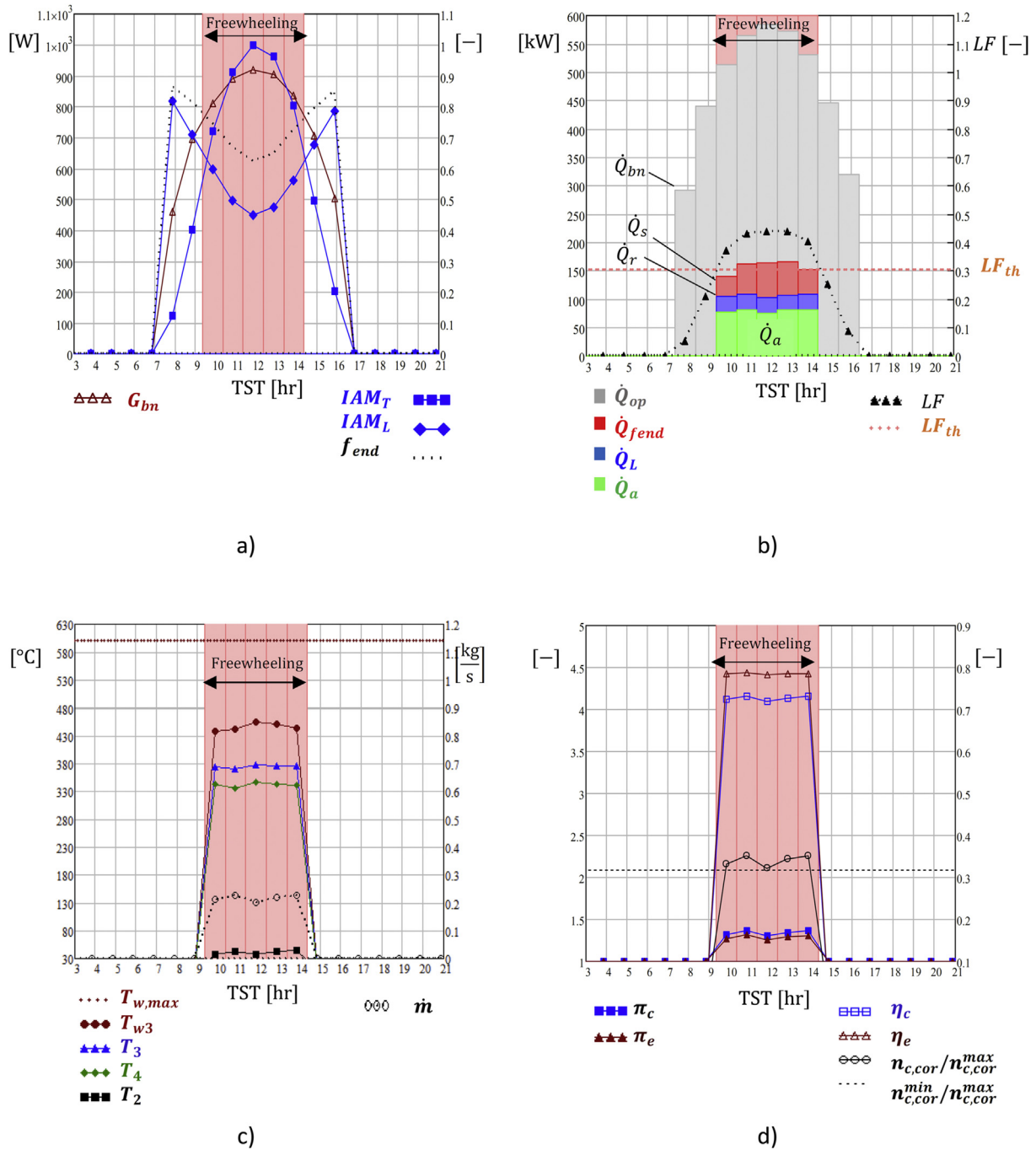


Fig. 10. T-SAH performances vs. true solar time TST during a clear winter day, Madrid (Spain).

$LF_{th} \cong 0.3$  is still valid. Fig. 10(c)–(d) confirms that the turbocharger is operating with a lower mass flow rate in winter than in summer, as well as with a lower  $\pi_c$ . Nevertheless, the self-regulation of the turbocharger allows delivering hot air at a fairly steady temperature around 330 °C.

### 3.2. Typical year

Extending the simulation all over the TMY allows a complete availability profile, whose results Fig. 11 depicts. As mentioned in Section 2.3, turbocharger freewheeling can be achieved across a large portion of the concentrated solar irradiance range expected

during the year, excluding low solar irradiance conditions. This issue is evident in Fig. 11(a) that displays the load factor  $LF = \dot{q}_s \dot{q}_{s,peak}^{-1}$  for each hour of the year across a TMY and the corresponding state of the T-SAH, either freewheeling (ON), or shut down (OFF) if freewheeling is not achievable. The approximate threshold  $LF_{th} \cong 0.3$ , predicted in Section 2.3 as a low power cut-off, seems confirmed across the whole year. Its effect on monthly working hours varies remarkably, as it is evident in Fig. 11(b), where monthly ON and OFF daylight hours are reported. The operative hours (ON) over the total monthly daylight hours drop in the winter season due to lower irradiance. During the OFF hours the solar power potentially available at the receiver  $\dot{Q}_r$ , Eq. (49), is relatively

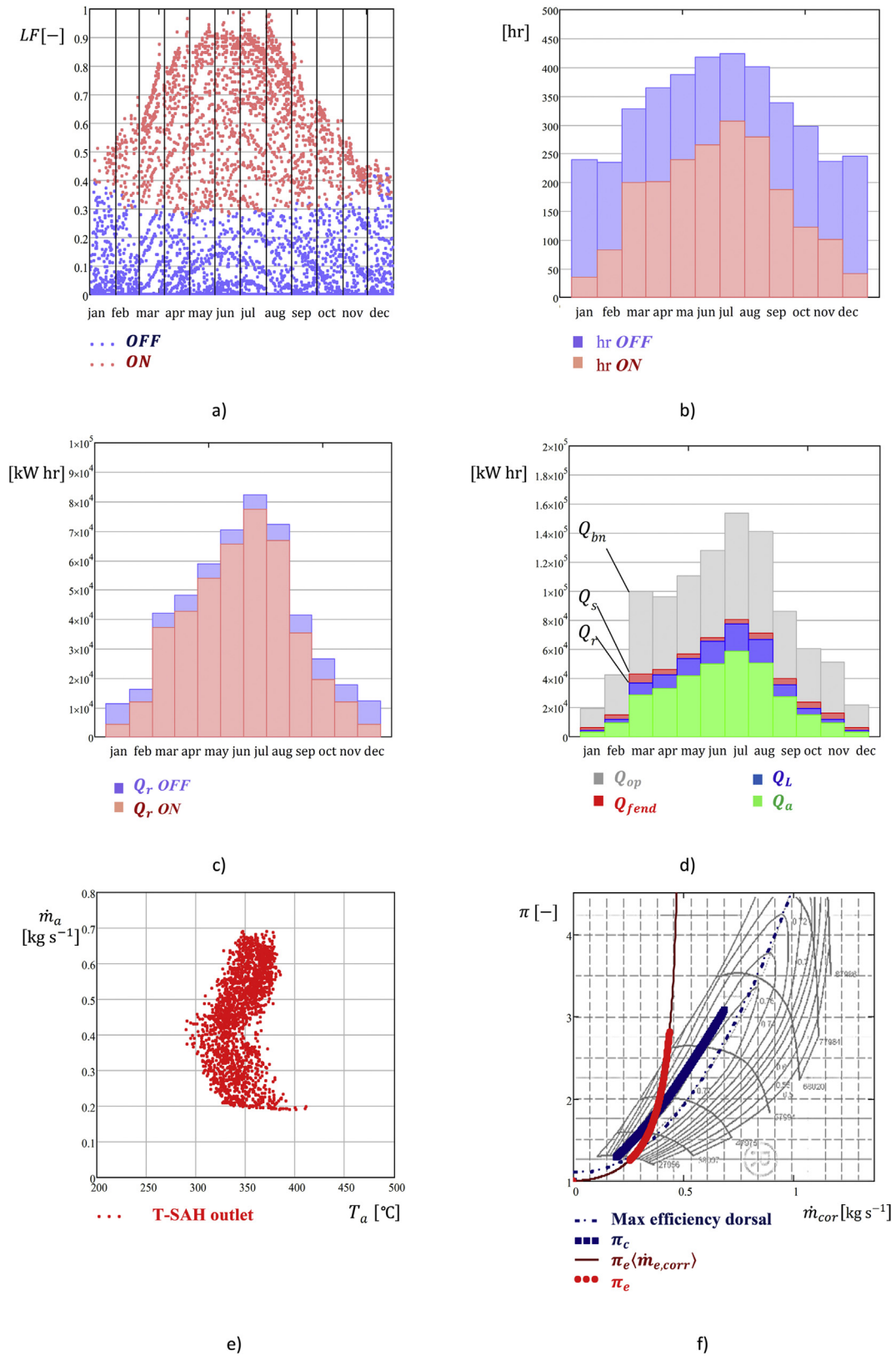


**Fig. 11.** T-SAH simulation results all over the year. a) concentrating solar irradiance range. b) operating hours per month. c) Energy delivered and not delivered per month. d) Energy contributions. e) T-SAH output. f) turbocharger operating parameters.

low, and therefore the energy not exploited by the T-SAH  $Q_{r,OFF}$  in the whole TMY is around 14% of the overall amount of energy available  $Q_{r,TOT} = Q_{r,ON} + Q_{r,OFF}$ . Fig. 11(c) reports  $Q_{r,ON}$  and  $Q_{r,OFF}$  on a monthly basis. The T-SAH could operate for 2060 h per year, corresponding to 52% of daylight yearly hours and 72% of yearly hours with appreciable concentrating irradiance, thus, higher than 10% of  $\dot{q}_{s,peak}$ .

Fig. 11(d) reports the T-SAH performances in terms of monthly energy contributions. Thermal energy delivered to the airflow sums the hourly energy contributions from the first to the last  $i$  hour of the month where T-SAH is ON,  $Q_a = \sum \dot{Q}_a \cdot h$ . Thermal losses  $Q_L = \sum \dot{Q}_L \cdot h$ , as well as optical end losses  $Q_{fend} = \sum \dot{Q}_{fend} \cdot h$  were evaluated. Normal direct (beam) solar energy available is computed considering the operating hours of T-SAH,  $Q_{bn} = \sum \dot{Q}_{bn} \cdot h$ . Both concentrated energy on the focal line,  $Q_s = \sum \dot{Q}_s \cdot h$ , and on the receiver  $Q_r = Q_s - Q_{fend}$  are indicated, as well as optical losses  $Q_{op} = Q_{bn} - Q_s$ . Along the year, the T-SAH delivered 330 MW hr of thermal energy.

Fig. 11(e) depicts a more detailed screening of the T-SAH output, in terms of  $\dot{m}$  against the corresponding air delivery temperature  $T_a = T_4$ . As expected, the delivery temperature varies in the range of  $300^\circ\text{C} < T_a < 400^\circ\text{C}$  according to the aim of the technology proposed. The mass flow rate varies in a range of  $0.2 \text{ kg s}^{-1} < \dot{m} < 0.7 \text{ kg s}^{-1}$ .

Fig. 11(f) displays the compressor and turbine working points on their maps for the whole TMY. The compressor works within the allowed speed range, and the mass flow rate does not exceed the surge and choke limits, besides operating near the highest-efficiency dorsal line. It was estimated that only 15% of working hours  $T_{w3} > 550^\circ\text{C}$ , giving a significant safety margin to the thermal limit. During peaks of power,  $T_{w3}$  do not overcome.  $T_{w,max} = 600^\circ\text{C}$ .

### 3.3. Integration with SAH

As discussed above, the T-SAH is not able to operate correctly at low solar power input, as seen for the present case roughly for  $LF <$

0.3, mainly occurring during winter months. A possibility to increase the annual hot air production exploiting the solar field also in T-SAH OFF conditions arises by modifying the layout of Fig. 1 into a simple SAH configuration. This means temporarily bypassing the turbocharger from the circuit and pumping the airflow through the solar field using the auxiliary compressor  $ac$ . Air exits the U-loop and it is directly delivered to the user at the temperature  $T_3 = T_a$  and atmospheric pressure. In fact, the low concentrated irradiance requires a relatively low mass flow rate to control the outlet temperature, Eq. (9). As a consequence, the total pressure loss across the U-loop  $\Delta p_{nr,t}$  is low, requiring a modest pumping power  $\dot{W}_{ac}$  to the auxiliary compressor/fan, Eq. (23),  $\pi_{ac} = 1 + \Delta p_{nr,t}/p_{amb}$ .

Assuming that the electrical driven auxiliary compressor is capable of continuous mass flow rate control, the desired temperature outlet  $T_a = 300^\circ\text{C}$  can be achieved in the range of low irradiance conditions, where T-SAH is not able to operate  $LF < \sim 0.3$ . Below  $LF < 0.1$ , solar power is assumed to be too low to run the concentrating solar plant, so that SAHs is OFF.

Integrating the T-SAH operation with the SAH mode for low irradiance conditions results in a higher number of working hours per month, as reported in Fig. 12(a), showing thermal performances in terms of monthly energy contribution. Energy consumed by the auxiliary compressor for air pumping in SAH mode  $W_{ac}$  is moderate, corresponding to the very low percentage of solar energy gain by air in the corresponding month  $Q_a$ , Fig. 12(b). For the 72% of exploitable sunny hours with  $LF > 0.1$ , the system works as T-SAH and the rest of the time as SAH. The annual energy delivered increases 13.3% thanks to the SAH integration, reaching 374 MW hr, and the annual working hours grow 38% with respect to the only T-SAH mode. The combination of the two modes allows exploiting the 97% of annual energy available at the receiver tube.  $Q_{r,TOT}$ .

Several performance parameters on yearly basis are reported in Table 5. The solar field average optical efficiency over the yearly working hours  $\bar{\eta}_{op} = Q_s/Q_{bn}$  together with yearly optical end losses factor  $\bar{f}_{end} = Q_r/Q_s$ , determine the global optical efficiency  $\bar{\eta}_{opg} = \bar{\eta}_{op}\bar{f}_{end} = Q_r/Q_{bn}$ . Yearly averaged thermal efficiency is defined as  $\bar{\eta}_{th} = Q_a/Q_r$  and accounts for thermal losses from the

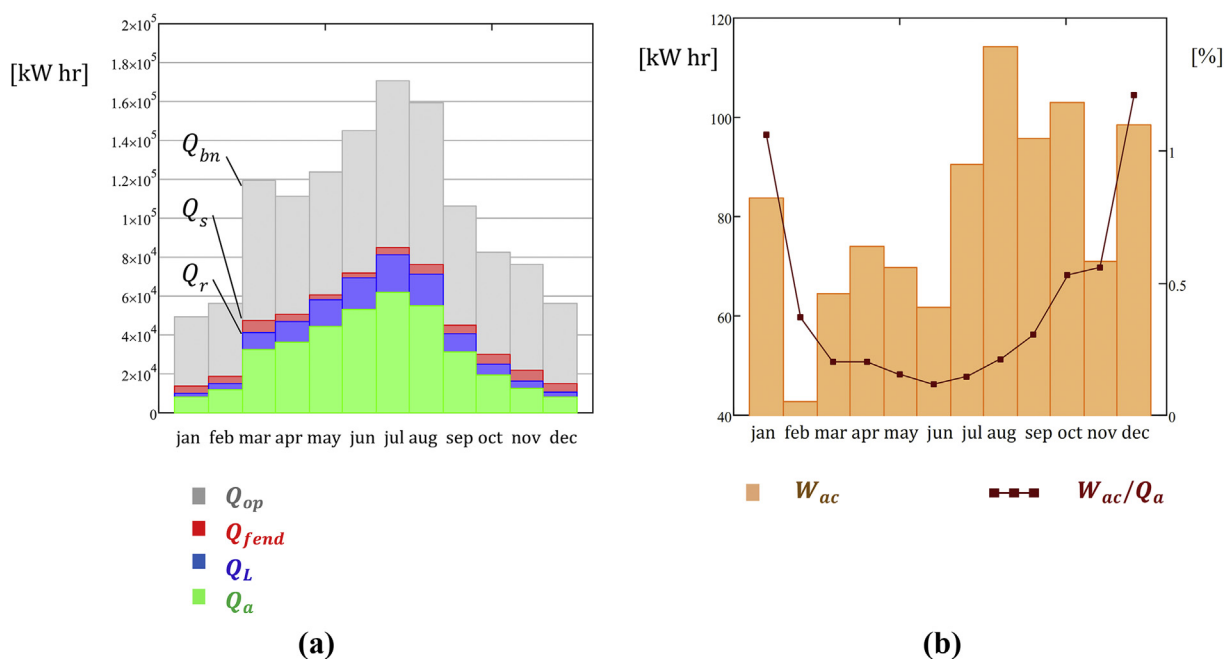


Fig. 12. (a). T-SAH integrated with SAH for low solar power: monthly energy contributions. (b). T-SAH integrated with SAH for low solar power: auxiliary compressor consumption.

**Table 5**  
Yearly performance parameter for T-SAH and T-SAH\* (T-SAH integrated with SAH).

Yearly Value	Unit	T-SAH	T-SAH*
$h_{ON}$	h	2060	2858
$Q_a$	MW h y <sup>-1</sup>	330	374
$Q_a/A_{tot}$	kW h y <sup>-1</sup> m <sup>-2</sup>	521.6	590.5
$Q_{bn}$	MW h y <sup>1</sup>	1012	1256
$\bar{\eta}_{op} = Q_s/Q_{bn}$	-	0.468	0.427
$\bar{f}_{end} = Q_r/Q_s$	-	0.909	0.902
$\bar{\eta}_{opg} = \bar{\eta}_{op}\bar{f}_{end}$	-	0.426	0.386
$\bar{\eta}_{th} = Q_a/Q_r$	-	0.767	0.772
$\bar{\eta}_a = Q_a/Q_{bn}$	-	0.327	0.298

collector tubes and piping. The global efficiency of solar air heating results  $\bar{\eta}_a = \frac{Q_a}{Q_{bn}} = \bar{\eta}_{opg}\bar{\eta}_{th}$ . They are estimated for T-SAH as well as for the T-SAH integrated with SAH (T-SAH\*) over the respective operating yearly hours. For the T-SAH\*  $\bar{\eta}_{op} = 0.427$  and  $\bar{f}_{end} = 0.902$  gives a global optical efficiency of  $\bar{\eta}_{opg} = 0.386$ . Thermal efficiency results  $\bar{\eta}_{th} = 0.772$ , giving an air heating efficiency of  $\bar{\eta}_a = 0.298$ . These figures are close to the ones attained by similar solar technologies. Although the usage of the turbocharger and the air as HTF difficult the comparison with similar plants, the optical and thermal efficiency obtained results following other linear Fresnel facilities reported in the literature. Ref. [16] simulated using commercial code a linear Fresnel field of 268.6 m<sup>2</sup> (36.1 deg N latitude), obtaining an average yearly optical efficiency of 0.379 and thermal efficiency of 0.858, which corresponds to a global efficiency of 0.325. Ref. [38] obtained a yearly global efficiency of 0.39 simulating a large LFC solar field of 6602 m<sup>2</sup> (38.1 deg N latitude) at moderate temperatures.

#### 4. Conclusions

An innovative concept for Turbo-assisted Solar Air Heater (T-SAH) using concentrating linear Fresnel collectors assisted by an automotive turbocharger was scrutinized in this study. Air is heated inside the solar receiver tube in an open-to-atmosphere circuit, avoiding the usage of both a primary heat transfer fluid and any heat exchanger. Thanks to a Brayton cycle configuration the T-SAH can provide hot air at medium temperature, without external energy consumption for pumping. A comprehensive mathematical model was implemented for detailed performance analysis of a medium scale T-SAH facility for industrial applications using off-the-shelf components and real meteorological data.

A 633.6 m<sup>2</sup> solar field of LFCs was coupled to an off-the-shelf turbocharger unit to achieve the best matching for the considered location of Madrid (Spain). The T-SAH performances were simulated for typical days in summer and winter, as well as along the typical meteorological year.

The results showed that the T-SAH can deliver 330 MW h per year of thermal power, supplying hot air in the range of 300 °C–400 °C without any external energy consumption for air pumping during 2060 h of the year with no storage. This is possible due to the beneficial self-adjusting operation of the turbocharger.

Only for very low solar irradiance, the T-SAH is not able to fulfil the turbocharger freewheeling operation, which occurred during winter months as well as in the early morning and late afternoon hours every day. Under this condition, using the system in SAH mode would increase the annual energy yield up to 374 MW h. Other options can be considered in further research, including external heat source backup, either from biofuel or renewable electricity, as well as from any thermal storage unit. Moreover, for better matching further work can consider in-parallel switchable

turbochargers and/or variable geometry turbines to cope with lower sun irradiances.

#### Credits

Antonio Famiglietti: Conceptualization, Methodology, Software, Validation, Investigation, Formal analysis, Writing - Original Draft, Writing - Review & Editing; Antonio Lecuona: Conceptualization, Methodology, Validation, Investigation, Writing - Review & Editing, Supervision, Project administration, Resources; Mercedes Ibarra: Methodology, Validation, Writing - Review & Editing; Javier Roa: Validation, Project administration, Resources.

#### Declaration of competing interest

The authors declare that they have no known competing financial interests or personal relationships that could have appeared to influence the work reported in this paper.

#### Acknowledgments

This research was supported by the Industrial Ph.D. program of Comunidad de Madrid, Spain (BOCM Reference IND2017/AMB7769).

Dr. Mercedes Ibarra acknowledges the generous financial support provided by CORFO (Corporación de Fomento de la Producción) under the project 13CEI2-21803.

#### Nomenclature

##### Latin

$A$	Aperture surface area [m <sup>2</sup> ]
$ac$	Auxiliary compressor
$B$	Parameter equation of time
$c_e$	Turbine flow map fitting coefficient
$c_p$	Air constant $p$ specific heat capacity [J kg <sup>-1</sup> °C <sup>-1</sup> ]
$C_U$	Coefficient for polynomial fitting of $U_L$
$D$	Inner diameter of the receiver tube [m]
$E$	Correction equation of time [min]
$F'$	Collector efficiency factor [-]
$F_R$	Collector heat removal factor [-]
$f$	Darcy friction coefficient [-], $f$ Function
$f_{end}$	Optical end losses factor [-]
$G_{bn}$	Normal beam irradiance [W m <sup>-2</sup> ]
$h_a$	Air heat transfer coefficient [W m <sup>-2</sup> °C <sup>-1</sup> ]
$h_{amb}$	Insulation to Air heat transfer coefficient [W m <sup>-2</sup> °C <sup>-1</sup> ]
$H_m$	Receiver distance from reflectors plane [m]
$IAM$	Incidence angle modifier [-]
$i$	Specific enthalpy [J kg <sup>-1</sup> ]
$IR$	Interpolation ratio [-]
$J_T$	Turbocharger moment of inertia [kg m <sup>2</sup> ]
$K$	Concentrated pressure losses coefficient [-]
$k$	Thermal conductivity [W m <sup>-1</sup> °C <sup>-1</sup> ]
$k_e$	Turbine flow map fitting coefficient
$k_{ij}$	Coefficients fitting coefficient of compressor flow map
$L$	Length [m]
$LF$	Load factor $\dot{q}_s/\dot{q}_{s,peak}$
$LST$	Local standard time [hr]
$Ma$	Mach number [-]
$\dot{m}$	Air mass flow rate [kg s <sup>-1</sup> ]
$n$	Rotating speed [rpm]
$n_d$	Day of the year
$n_p$	Number parallel U-loops

$n_s$	Number of modules in series in a U-loop	$i$	Hour of the year
$n_1, n_2, n_3$	Connection tubes	$in$	Inlet
$n_m$	Number of mirror strips of LFC module	$ins$	Insulation
$n_e$	Number of discretization elements of $L_{row}$	$k$	Kinetic energy component
$P$	Receiver tube cross-section perimeter [m]	$L$	Thermal losses to ambient
$Pr$	Prandtl number [–]	$loc$	Location
$p$	Pressure [Pa]	$m$	LFC module
$\dot{Q}$	Thermal power [W]	$n$	Connection tube
$Q$	Thermal energy [J]	$net$	Net balance
$\dot{q}_s$	Incident concentrated solar irradiance [ $W\ m^{-2}$ ]	$norm$	Normalized
$\dot{q}_u$	Thermal power flux to air [ $W\ m^{-2}$ ]	$ou$	Outlet
$Re$	Reynolds number [–]	$ON$	T-SAH operative
$R_g$	Gas constant = $R/M_g$ [ $m^2\ s^{-2}\ ^\circ C^{-1}$ ]	$OFF$	T-SAH shut off
$SR$	Tip speed ratio [–]	$op$	Optical
$T$	Temperature [K, $^\circ C$ ]	$opt$	Optimum
$TST$	True solar time [hr]	$peak$	Peak
$U_c$	Tip blade speed compressor [ $m\ s^{-1}$ ]	$r$	Receiver
$U_e$	Tip blade speed turbine [ $m\ s^{-1}$ ]	$row$	LFC series row
$U_L$	Thermal losses coefficient of the receiver [ $W\ m^{-2}\ K^{-1}$ ]	$ref$	Reference operation
$U_{Ln}$	Thermal losses coefficient of insulated tubes [ $W\ m^{-2}\ K^{-1}$ ]	$s$	Solar
$UTC$	Standard time zone of Universal Coordinate Time	$t$	Stagnation variable
$v$	Average airflow velocity [ $m\ s^{-1}$ ]	$tot$	Total
$\dot{W}$	Power [W]	$T$	Turbocharger
$W_a$	Rectangular aperture total width [m]	$u$	Useful
$w_a$	Aperture width of a single mirror of LFC [m]	$w$	Wall
		0	Inlet from atmosphere
		1	Compressor inlet
		2	Compressor outlet
		3	Turbine inlet
		4	Turbine outlet
<b>Greek</b>		<b>Superscripts</b>	
$\alpha_s$	Solar elevation [rad]	$surge$	Surge limit
$\gamma$	Isentropic exponent [–]	$choke$	Choke limit
$\gamma_s$	Solar azimuth [rad]	$min$	Minimum
$\gamma_r$	LFC azimuth [rad]	$max$	Maximum
$\delta$	Sun declination [[rad]]	$th$	Threshold
$\rho$	Density [ $kg\ m^{-3}$ ]	$pt$	Potential
$\eta_{op0}$	Maximum optical efficiency [–]		
$\lambda_{st}$	Local time zone standard meridian longitude west [deg]	<b>Acronyms</b>	
$\lambda_{loc}$	Collector location longitude west [deg]	AC	Air Collector
$\eta_m$	Mechanical efficiency of turbocharger [–]	ETC	Evacuated Tube Collector
$\eta$	Total to total isentropic efficiency [–]	HTF	Heat Transfer Fluid
$\psi_c$	Compressor head parameter [–]	IAM	Incident Angle Modifier
$\varphi_c$	Compressor non-dimensional flow parameter [–]	LFC	Linear Fresnel collector
$\Phi_{loc}$	Latitude north [deg]	OAC	Open to Atmosphere Circuit
$\pi$	Pressure ratio [–]	PTC	Parabolic Trough Collector
$\mu$	Dynamic viscosity [ $kg\cdot m^{-1}\ s^{-1}$ ]	SAH	Solar Air Heater
$\nu$	Kinematic viscosity [ $m^2\ s^{-1}$ ]	SHC	Solar Heating Collectors
$\theta_L$	Longitudinal angle [rad]	SHIP	Solar Heat for Industrial Processes
$\theta_T$	Transversal angle [rad]	T-SAH	Turbo-assisted Solar Air Heater
$\theta_i$	Longitudinal component of incident angle [rad]	TMY	Typical Meteorological Year
$\theta_z$	Solar zenith angle [rad]		
$\tau$	Time [s]	<b>Others</b>	
$\omega$	Angular speed [ $rad\ s^{-1}$ ]	$\langle \rangle$	Functional dependence.
$\omega_s$	Hour angle [rad] (negative in the morning)		
<b>Subscripts</b>		<b>Appendix</b>	
$a$	Air		
$amb$	Ambient		
$atm$	Atmospheric		
$bn$	Normal beams		
$c$	Compression. Compressor		
$cor$	Corrected		
$e$	Expansion. Turbine		
$ex$	Receiver tube external surface		
$f$	Friction		
$f_{end}$	End optical losses factor		

Sun position at any time for the considered location is obtained using well-known equations [24]. True solar time TST is obtained from local standard time applying the corrections as in Eqs. (A.2 - A.4). Incident solar angle  $\theta_z$  results as in Eq. (A.6) from solar hour angle  $\omega_s$ , Eq. (A.5), and solar declination  $\delta$ , Eq. (A.1). Solar elevation  $\alpha_s$  and azimuth  $\gamma_s$  results from Eq. (A.7) and Eq. (A.8).

$$\delta = 23.45 \sin\left(\frac{2\pi}{365}\right)(284 + n_d) \quad (\text{A.1})$$

$$E = 229.18[0.000075 + 0.001868 \cos(B) - 0.032077 \sin(B) - 0.014615 \cos(2B) - 0.04089 \sin(2B)] \quad (\text{A.2})$$

$$B = \frac{(n_d - 1)2\pi}{365} \quad (\text{A.3})$$

$$TST = 4(\lambda_{st} - \lambda_{loc}) + E + LST; \lambda_{st} = -UTC \frac{2\pi}{24} \quad (\text{A.4})$$

$$\omega_s = \frac{2\pi}{24}(TST - 12 \text{ h}) \quad (\text{A.5})$$

$$\theta_z = \cos^{-1}[\cos(\Phi_{loc})\cos(\delta)\cos(\omega_s) + \sin(\Phi_{loc})\sin(\delta)] \quad (\text{A.6})$$

$$\alpha_s = \frac{\pi}{2} - \theta_z \quad (\text{A.7})$$

$$\gamma_s = \text{sign}(\omega_s) \left| \cos^{-1} \left( \frac{(\sin(\Phi_{loc})\cos(\theta_z) - \sin(\delta))}{\sin(\theta_z)\cos(\Phi_{loc})} \right) \right| \quad (\text{A.8})$$

## References

- [1] International Energy Agency. Key world energy statistics 2019. 2018.
- [2] IEA. World energy statistics 2016. n.d. [www.iea.org/statistics/](http://www.iea.org/statistics/).
- [3] International renewable energy agency (IRENA) (n.d.). [www.irena.org](http://www.irena.org).
- [4] Sharma AK, Sharma C, Mullick SC, Kandpal TC. Solar industrial process heating: a review. *Renew Sustain Energy Rev* 2017;78:124–37. <https://doi.org/10.1016/j.rser.2017.04.079>.
- [5] Pirasteh G, Saidur R, Rahman SMA, Rahim NA. A review on development of solar drying applications. *Renew Sustain Energy Rev* 2014;31:133–48. <https://doi.org/10.1016/j.rser.2013.11.052>.
- [6] Wu ZH, Hu YJ, Lee DJ, Mujumdar AS, Li ZY. Dewatering and drying in mineral processing industry: potential for innovation. *Dry. Technol* 2010;28:834–42. <https://doi.org/10.1080/07373937.2010.490485>.
- [7] Kumar L, Hasanuzzaman M, Rahim NA. Global advancement of solar thermal energy technologies for industrial process heat and its future prospects: a review. *Energy Convers Manag* 2019;195:885–908. <https://doi.org/10.1016/j.enconman.2019.05.081>.
- [8] Farjana SH, Huda N, Mahmud MAP, Saidur R. Solar process heat in industrial systems – a global review. *Renew Sustain Energy Rev* 2018;82:2270–86. <https://doi.org/10.1016/j.rser.2017.08.065>.
- [9] Kabeel AE, Hamed MH, Omara ZM, Kandael AW. Solar air heaters: design configurations, improvement methods and applications – a detailed review. *Renew Sustain Energy Rev* 2017;70:1189–206. <https://doi.org/10.1016/j.rser.2016.12.021>.
- [10] Ship Database (n.d.). <http://ship-plants.info/>.
- [11] Rehman S, Ahmad A, Alhems LM, Rafique MM. Experimental evaluation of solar thermal performance of linear Fresnel reflector. *J Mech Sci Technol* 2019;33:4555–62. <https://doi.org/10.1007/s12206-019-0852-6>.
- [12] Famiglietti A, Lecuona-Neumann A, Nogueira J, Rahjoo M. Direct solar production of medium temperature hot air for industrial applications in linear concentrating solar collectors using an open Brayton cycle. *Viability analysis* 2020;169. <https://doi.org/10.1016/j.applthermaleng.2020.114914>.
- [13] Schnitzer H, Brunner C, Gwehenberger G. Minimizing greenhouse gas emissions through the application of solar thermal energy in industrial processes. *J Clean Prod* 2007;15:1271–86. <https://doi.org/10.1016/j.jclepro.2006.07.023>.
- [14] Bellos E. Progress in the design and the applications of linear Fresnel reflectors – a critical review. *Therm. Sci. Eng. Prog.* 2019;10:112–37. <https://doi.org/10.1016/j.tsep.2019.01.014>.
- [15] Heimsath A, Bern G, Van Rooyen D, Nitz P. Quantifying optical loss factors of small linear concentrating collectors for process heat application. *Energy Procedia* 2014;48:77–86. <https://doi.org/10.1016/j.egypro.2014.02.010>.
- [16] Giostri A, Binotti M, Silva P, Macchi E, Manzolini G. Comparison of two linear collectors in solar thermal plants: parabolic Trough vs Fresnel. *Energy Sustain.* 2011;54686:621–30.
- [17] Karathanasis S. Linear Fresnel reflector systems for solar radiation concentration. 2019. <https://doi.org/10.1007/978-3-030-05279-9>.
- [18] Solatom. Solar steam for industrial processes (n.d.). <http://www.solatom.com/>.
- [19] Eck M, Hirsch T, Feldhoff JF, Kretschmann D, Dersch J, Gavilan Morales A, Gonzalez-Martinez L, Bachelier C, Platzer W, Riffelmann KJ, Wagner M. Guidelines for CSP yield analysis - optical losses of line focusing systems; definitions, sensitivity analysis and modeling approaches. *Energy Procedia* 2014;49:1318–27. <https://doi.org/10.1016/j.egypro.2014.03.141>.
- [20] Hongn M, Larsen SF, Gea M, Altamirano M. Least square based method for the estimation of the optical end loss of linear Fresnel concentrators. *Sol Energy* 2015;111:264–76. <https://doi.org/10.1016/j.solener.2014.10.042>.
- [21] Forristall R. Heat transfer analysis and modeling of a Parabolic Trough solar receiver implemented in engineering equation solver. 2003. p. 164. <https://doi.org/NREL/TP-550-34169>.
- [22] Burkholder F, Kutscher C. Heat-loss testing of solel's UVAC3 Parabolic Trough receiver. *NREL Tech. Rep. TP- 2008;550-423:19*.
- [23] Incropera FP, DeWitt DP. Fundamentals of heat and mass transfer. 1996. p. 890. <https://doi.org/10.1016/j.applthermaleng.2011.03.022>.
- [24] Duffie JA, Beckman WA, McGowan J. Solar engineering of thermal processes. 1985. <https://doi.org/10.1119/1.14178>.
- [25] Muñoz-Anton J, Biencinto M, Zarza E, Díez LE. Theoretical basis and experimental facility for parabolic trough collectors at high temperature using gas as heat transfer fluid. *Appl Energy* 2014;135:373–81. <https://doi.org/10.1016/j.apenergy.2014.08.099>.
- [26] Guzzella L, Onder CH. Introduction to modeling and control of internal combustion engine systems. 2010. <https://doi.org/10.1007/978-3-642-10775-7>.
- [27] Jensen JP, Kristensen AF, Sorenson SC, Houbak N, Hendricks E. Mean value modeling of a small turbocharged diesel engine. *SAE Tech. Pap.* 1991. <https://doi.org/10.4271/910070>.
- [28] Frei SA, Guzzella L, Onder CH, Nizzola C. Improved dynamic performance of turbocharged SI engine power trains using clutch actuation. *Contr Eng Pract* 2006;14:363–73. <https://doi.org/10.1016/j.conengprac.2005.01.014>.
- [29] Eriksson L. Modeling and control of TC SI and DI engines. *Oil Gas Sci Technol* 2008;63:9–19. <https://doi.org/10.2516/ogst>.
- [30] Sorenson SC, Hendricks E, Magnusson S, Bertelsen A. Compact and accurate turbocharger modelling for engine control. *SAE Tech. Pap.* 2005;2005. <https://doi.org/10.4271/2005-01-1942>.
- [31] Galindo J, Tiseira A, Navarro R, Tari D, Tartoussi H, Guilain S. Compressor efficiency extrapolation for 0D-1D engine simulations. *SAE Tech. Pap* 2016. <https://doi.org/10.4271/2016-01-0554>.
- [32] Casey M, Robinson C. A method to estimate the performance map of a centrifugal compressor stage. *J Turbomach* 2012;135:1–10. <https://doi.org/10.1115/1.4006590>.
- [33] Payri F, Serrano JR, Fajardo P, Reyes-Belmonte MA, Gozalbo-Belles R. A physically based methodology to extrapolate performance maps of radial turbines. *Energy Convers Manag* 2012;55:149–63. <https://doi.org/10.1016/j.enconman.2011.11.003>.
- [34] Zhu S, Deng K, Liu S. Modeling and extrapolating mass flow characteristics of a radial turbocharger turbine. *Energy* 2015;87:628–37. <https://doi.org/10.1016/j.energy.2015.05.032>.
- [35] Fang X, Dai Q, Yin Y, Xu Y. A compact and accurate empirical model for turbine mass flow characteristics. *Energy* 2010;35:4819–23. <https://doi.org/10.1016/j.energy.2010.09.006>.
- [36] Habte A, Stoffel T, Perez R, Myers D, Gueymard C, Blanc P, Wilbert S. Best practices handbook for the collection and use of solar resource data for solar energy applications. second ed. 2017. p. 2.1–2.22 Nrel [www.nrel.gov/publications](http://www.nrel.gov/publications).
- [37] EU Science HUB, PVGIS (n.d.). <https://ec.europa.eu/jrc/en/pvgis>.
- [38] Buscemi A, Panno D, Ciulla G, Beccali M, Lo Brano V. Concrete thermal energy storage for linear Fresnel collectors: exploiting the South Mediterranean's solar potential for agri-food processes. *Energy Convers Manag* 2018;166:719–34. <https://doi.org/10.1016/j.enconman.2018.04.075>.